

Aus der Universitätsklinik für Thorax-, Herz-, und Gefäßchirurgie Tübingen

Ärztlicher Direktor: Professor Dr. C. Schlensak

Sektion Medizinische Werkstoffkunde und Technologie

**Photocatalytic antibacterial effects on TiO₂-anatase
upon UV-A and UV-A/VIS threshold irradiation**

**Inaugural- Dissertation
zur Erlangung des Doktorgrades
der Zahnheilkunde**

**der Medizinischen Fakultät
der Eberhard Karls Universität
zu Tübingen**

vorgelegt von

Wu Yanyun

2017

Dekan: Professor Dr. B. Autenrieth

1.Berichterstatter: Professor Dr. J. Geis-Gerstorfer

2.Berichterstatter: Privatdozentin Dr. E. Engel

Tag der Disputation: 27.02.2017

<u>1. Introduction.....</u>	<u>1</u>
1.1 Implant materials.....	1
1.1.1 Titanium and its alloys.....	1
1.1.2 Titanium modification.....	2
1.2. Peri-implantitis.....	4
1.2.1 Etiology of peri-implantitis.....	4
1.2.2 The treatment of peri-implantitis.....	5
1.3 Photocatalysis.....	7
1.3.1 General concept.....	7
1.3.2 Photocatalysis and anatase.....	8
1.3.3 The photocatalytic bactericidal effect.....	10
1.4 Quartz crystal microbalance with dissipation.....	11
1.5 Aim of the study.....	13
<u>2. Materials and methods.....</u>	<u>14</u>
2.1 Preparation of samples.....	14
2.2 Surface Characterization.....	16
2.3 Human sterile saliva.....	16
2.4 Bacteria suspension.....	16
2.5 Protocols of light irradiation.....	17
2.6 QCM tests.....	18
2.7 Hydrodynamic Calculations.....	22
2.8 Live/Dead staining and microscopic examination.....	24
2.9 Image analysis.....	25
2.10 Statistical analysis.....	26
<u>3. Results.....</u>	<u>26</u>

3.1 Surface properties.....	26
3.2 QCM online experiments.....	27
3.3 Microscopic analysis after Live/Dead staining.....	32
3.4 Image evaluation.....	35
<u>4. Discussion.....</u>	<u>38</u>
4.1 Analysis of the photocatalytic antibacterial performance.....	38
4.1.1 Analysis of the experimental results on Ti surface.....	38
4.1.2 Analysis of the experimental results on anatase surface (irradiation with higher flow rate 2700 $\mu\text{l min}^{-1}$).....	39
4.2 The influence of rinsing flow rate.....	43
<u>5. Conclusions.....</u>	<u>44</u>
<u>6. Summary.....</u>	<u>45</u>
<u>7. Zusammenfassung.....</u>	<u>46</u>
<u>8. References.....</u>	<u>48</u>
<u>9. Erklärung zum Eigenanteil.....</u>	<u>59</u>
<u>10. Publication of the content of the dissertation.....</u>	<u>60</u>
<u>11. Acknowledgment.....</u>	<u>60</u>

Abbreviation

Cp Ti	commercially pure titanium
OHI	oral hygiene instructions
CHX	chlorhexidine
PDT	photodynamic therapy
BOP	bleeding on probing
Ti	titanium
TiO ₂	titanium dioxide
UV	ultraviolet
ROS	reactive oxygen species
QCM-D	quartz crystal microbalance with dissipation
VIS	visible
HSA	human serum albumin
PBS	phosphate-buffered saline
<i>S. gordonii</i>	<i>Streptococcus gordonii</i>
OD	optical density
f	frequency
D	dissipation

E. coli

Escherichia coli

EPS

extracellular polymeric substances

F-D

Frequency-Dissipation

1. Introduction

1.1 Implant materials

1.1.1 Titanium and its alloys

After the introduction by Brånemark in the 1970s, dental implantation has become a popular treatment strategy for the replacement of missing teeth (Brånemark et al. 1977). To ensure the clinical outcome of implant therapy, the properties of implant materials are essential factors to take into consideration (Smith 1993). Generally speaking, the ideal implant material should be biocompatible, with adequate toughness, strength, corrosion, wear and fracture resistance (Parr et al. 1985).

Among the various implant materials, titanium (Ti) has been regarded as “gold standard” material for the fabrication of dental implants and the reported long-term clinical survival rates supported this application (Adell et al. 1990, Jemt et al. 1996, Niinomi 1998). There are six types of titanium available as implant biomaterials: four grades of commercially pure titanium (cp Ti) and two titanium alloys. The cp Ti materials, also called unalloyed titanium, are classified into Grade I, Grade II, Grade III and Grade IV. This gradation is related to the amount of oxygen residuals in the metal and higher amounts of oxygen are found from Grade I to IV. The two alloys are Ti-6Al-4V and Ti-6Al-4V-ELI (“extra-low interstitial”, a higher-purity version of Ti-6Al-4V) (Osman and Swain 2015). Titanium and its alloys have a good specific strength and acceptable corrosion resistance; then, the allergic evidence is relatively low; finally, the amorphous passive titanium oxide layer on the surface endows this material the best biocompatibility among metallic materials (Niinomi 2003).

1.1.2 Titanium modification

The high success rate of titanium dental implants for oral reconstruction has been attributed to its ability for osseointegration, which means a direct structural and functional connection between bone and implant and no intervening soft tissues (Brånemark et al. 1969). However, it is always challenging to ensure successful osseointegration in face of advanced bone resorption and poor bone quality. One way to solve this problem is to use implants with modified surfaces (Assender et al. 2002). It has been suggested that the physiochemical properties, crystal structure, and surface morphology of titanium oxide films on dental implant surfaces play an important role in the biocompatibility and osseointegration of implants (Bowers et al. 1992, Martin et al. 1995, Rupp et al. 2004, Busquim et al. 2010).

The process of biomolecular adsorption onto materials is regarded as a dynamic process modulated by the physico-chemical interactions between material surfaces and macromolecules (Puleo and Nanci 1999). At cellular level, some biological responses, such as the orientation and migration of cells and the cellular production of organized cytoskeletal arrangements, are supposed to be directly influenced by the surface topography (Flemming, Murphy et al. 1999). The osteoblast differentiation, proliferation and matrix production as well as the production of local growth factors and cytokines are affected by surface roughness (Martin, Schwartz et al. 1995, Kieswetter, Schwartz et al. 1996). Among the large amount of ways of surface modifications, anatase coatings on Ti surface has been regarded a promising way to enhance the interactions between the material and the surrounding biological environment (Sollazzo et al. 2007).

Besides, although there is good response between Ti-based materials and the human body, bacteria also may colonize on its surface resulting in biomaterial-centered infections, or, more specifically, in prosthetic implant infections, which might lead to prosthetic implant loosening and failure (Gristina, Naylor et al. 1988, Brady, Calhoun et al. 2009). It has been reported that the anatase surface could decrease the bacterial attachment in comparison with the amorphous titanium, while having no adverse effects on the normal cell metabolism (Del Curto et al. 2005). In a recent study by Lorenzetti M (Lorenzetti, Dogsa et al. 2015), the surface of titanium was hydrothermally treated to be coated with nanostructured anatase coatings. Using *Escherichia coli* (*E.coli*) as a model bacterium, the effects of surface topography, roughness, and charge on the bacterial adhesion were investigated. It has been found that the macroscopic surface topography and the microroughness influenced bacterial attachment. Macroscopic grooves provided a favorable place for bacterial deposit within the valleys, and the microscopic roughness determined the actual interaction surface between bacteria and the substrate. On the nontreated titanium, the so-called “interlocking” effect exists and resulted in high bacterial adhesion. In contrast, on the anatase-coated surface the distance between the microasperities was reduced by the nanocrystals and thus the contact area between the bacteria and the crystalline surface. Up to 50% less bacterial adhesion was observed on the anatase-coated samples in comparison to the nontreated titanium (Lorenzetti et al. 2015). In another study by Delcurto B. (Del Curto, Brunella et al. 2005), the crystalline anatase layer converted from the amorphous titanium oxide showed a stimulation of apatite precipitation. By using several kinds of bacteria from *Streptococcus*

strains for the bacterial adhesion study, the bacterial attachment showed a higher reduction on anatase surfaces compared with that on pure titanium. What's more, the crystalline surface also showed a stimulation of apatite precipitation when placed in simulated body fluid.

To sum up, anatase coating is a promising method for surface modification of titanium implants. In this study, we adopted the reactive pulse magnetron sputtering method to deposit crystalline anatase layers on the quartz crystal surface. Beside possible advantages discussed above, the main purpose to use anatase here as the surface modification on the samples is to evaluate photocatalytic antibacterial effects on this special semiconductor.

1.2 Peri-implantitis

1.2.1 Etiology of peri-implantitis

Although dental implantation has become a common therapy in different clinical situations, it also brought about some potential risks (Renvert et al. 2009). Peri-implant infections have become a rising complication after the surgical treatment (Lindhe and Meyle 2008, Zitzmann and Berglundh 2008). The term "peri-implantitis" was put forward decades ago to represent the infectious conditions of peri-implant tissues and was specifically utilized to describe the condition of non-reversible inflammation in adjacent tissues around osseointegrated implants, which might lead to the regression and loss of bone support (Heitz-Mayfield 2008, Mombelli et al. 2012).

Bacterial infections play the most important role in this peri-implant inflammation. Bacterial floras, which are associated with periodontitis and peri-implantitis, are found to be similar (Heydenrijk et al. 2002). Since the epithelial fibers around the implant are longitudinally directed and circumferential, they

cannot form tight connection with the implant body and, as a result, the bacteria are easier to get infiltrated and lead to infection. Excessive mechanical stress, complex design of the implant, and some local or systemic factors, such as diabetes mellitus, osteoporosis and smoking, are also important factors in the onset and development of peri-implantitis (Prathapachandran and Suresh 2012).

1.2.2 The treatment of peri-implantitis

Since the development of peri-implantitis can result in signs of inflammation, the destruction of surrounding bone structure, and further implant loss, it is important to investigate possible effective ways to deal with such cases (Esposito et al. 1999, Quirynen et al. 2002). In general, the treatment methods of peri-implantitis include nonsurgical and surgical ways. According to the review by Schwarz et al. (Schwarz et al. 2015), the treatment methods could be summarized as followed:

Nonsurgical treatment of peri-implantitis:

1. Alternative measures for biofilm removal:

Oral hygiene instructions (OHI) + mechanical debridement / ultrasonic device with polish / Er:YAG laser device / air abrasive device ± chlorhexidine (CHX) irrigation and CHX gel

2. Adjunctive antiseptic therapy:

OHI + mechanical debridement + matrix containing CHX chips

3. Adjunctive antibiotic therapy:

OHI + mechanical debridement ± CHX irrigation + local application of antibiotics

Surgical treatment of peri-implantitis:

1. Alternative measures for surface decontamination:

OHI + open flap surgery ± resective therapy + surface debridement ± decontamination by CHX

2. Adjunctive resective therapy:

Full mouth disinfection / mechanical debridement + resective therapy + decontamination by antibiotics

3. Adjunctive augmentative therapy

OHI + open flap surgery + mechanical debridement / air polishing + decontamination + autogeneous bone / bone substitute material + barrier membrane

Besides, nowadays, the photodynamic therapy (PDT) also served as a treatment protocol against peri-implantitis (Schaer et al. 2013, Bombeccari et al. 2013).

Considering the outcomes of these various ways treating peri-implantitis, it could be concluded that OHI combined with mechanical debridement was effective to treat peri-implantitis. However, since the configuration or morphology on the implant surfaces were often complex structured, the mechanical biofilm removal procedures might not access the whole exposed surface (Sahrmann et al. 2015). What's more, the mechanical debridement might lead to destruction of implant surface structure and introducing new scratches which might enhance bacterial adhesion. In the nonsurgical treatment of peri-implantitis, the adjunctive local antiseptic, antibiotic, laser or powder air polishing therapy were shown to improve the efficacy of treatments by reducing bleeding on probing (BOP) scores. But the nonsurgical methods failed to reduce the quantity of microbiota in peri-implantitis lesions. In the

surgical treatment protocols, it has indicated that the clinical, radiographical and microbiological outcomes were not influenced by the decontamination protocol and no conclusions on the superiority of augmentation treatment could be drawn out (Schwarz et al. 2015, Froum et al. 2016). Regarding PDT therapy, it could be applied as an adjunctive method of mechanical debridement in the cases of initial peri-implantitis. However, the complete recovering from the inflammation could not be achieved with this way alone (Bombeccari et al. 2013, Schaer et al. 2013). Based on these, it is also desirable to explore new possibilities to treat this complication and get rid of the pathogenic bacteria colonization effectively and harmlessly.

1.3. Photocatalysis

1.3.1 General concept

Photocatalysis is a term that combines the basic notion of a catalyst as a material that enhances the rate of a reaction to approach equilibrium without being consumed with the notion that the reaction is accelerated by photons (Langford 2012). Generally, photocatalysis occurs through photon absorption rather than by thermal activation, which is normal in conventional catalysis. It involves the absorption of light by a solid photocatalyst, and then the activation state of at least one reactant adsorbed on the catalyst surface would be modified, thus producing a new reaction path with a lower activation barrier than that for the thermal reaction proceeding in the absence of light (Howe 1998).

Today, semiconductor materials are usually selected as photocatalysts, due to their band gap structure. The band gap lies between the top of the valence band and the bottom of conduction band, while in metal the electronic state is

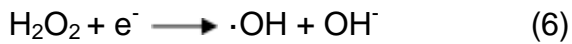
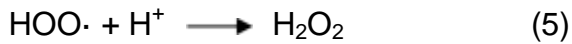
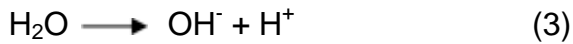
continuous and there's no such gap structure. When the photon energy of the irradiation light is equal to or more than its energy gap, an electron from the valence band will be excited to the conduction band. This movement of electrons forms negatively charged electron/positively charged hole pairs and the photoinduced electron and holes will be transferred to the semiconductor surface. When some electron donor or acceptors, e.g., water, oxygen, exist in the surrounding environment at the same time, oxidative and reduction reactions will undergo on the conduction band and on the valence band, respectively (Benedix et al. 2000).

1.3.2 Photocatalysis and anatase

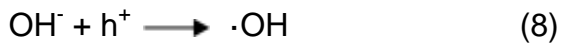
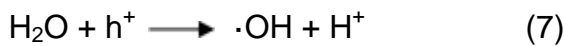
The concept photocatalysis can be traced back to the discovery of water splitting on titanium dioxide (TiO_2) electrodes by Fujishima and Honda (Fujishima and Honda 1972). Since then, a series of studies on TiO_2 or other semiconductor materials have been conducted aiming to utilize or improve their photocatalysis (Kaneva, Stambolova et al. 2010). So far, this property has already been applied in many fields, such as energy conversion, environmental purification, self-cleaning and antifogging surfaces (O'Regan and Gratzel 1991, Wang et al. 1998). With respect to biological and biomedical applications, the decomposition of organic compounds, antibacterial effects driven by photocatalysis, and an increase in hydrophilicity of biomaterial surfaces upon irradiation of these materials have also been extensively studied (Muszkat et al. 2002, Ditta et al. 2008, Hayashi et al. 2012). As described in 1.1.2, among the three crystalline forms of TiO_2 , anatase displays best bone-bonding ability and photocatalytic properties (Sclafani and Herrmann 1996, Barbour et al. 2009, Luttrell et al. 2014). Ultraviolet (UV) light

with a photon energy ($\lambda < 385 \text{ nm}$) exceeding the band gap of anatase of 3.2 eV can excite electrons into the valence band and leave holes in the conduction band. Furthermore, in the presence of O_2 and H_2O , these electrons and holes generate various active oxygen species which can decompose organic molecules through a series of oxidization reactions (Tran, Nosaka et al. 2006).

Specifically, the reduction reaction progresses in the conduction band (CB) and lead to the formation of superoxide radicals ($\text{O}_2^{\cdot-}$) (Equation. 2) and hydroxyl radicals ($\cdot\text{OH}$) (Equations. 3-6).



On the other hand, oxidation reactions occur on the valence band (VB) and lead to the formation of hydroxyl radicals (Equations. 7-8)



When these reactive oxygen species (ROS) have been formed, the oxidation of organic substances starts (Equation. 9)



Through these chain reactions, the organic compounds can be photocatalytically decomposed and transferred to inorganic substances (Figure 1).

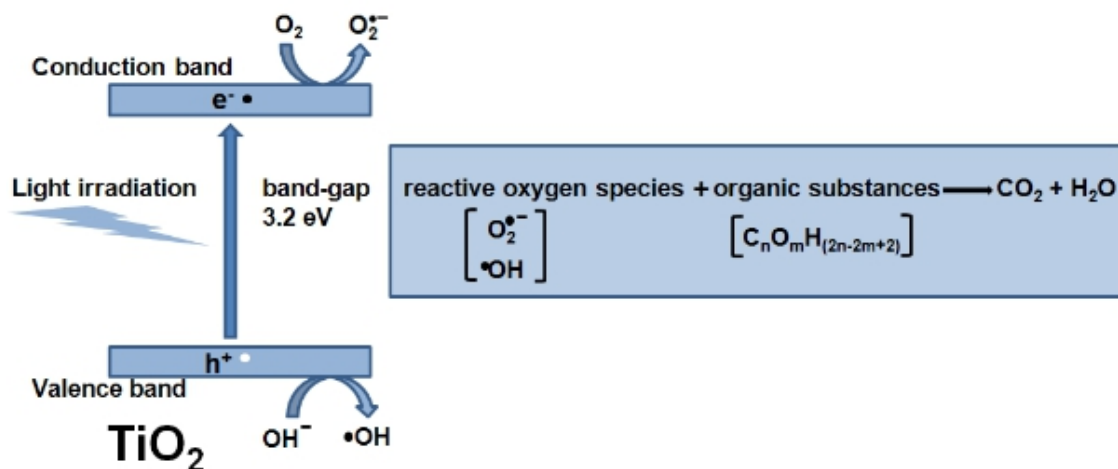


Figure 1: The basic mechanism of photocatalysis on TiO_2 surface

*This figure was modified from the image which was taken from:

http://sangakukan.jp/journal/journal_contents/2010/06/articles/1006-03-2/1006-03-2_earticle.html

1.3.3 The photocatalytic bactericidal effect

Matsunaga et al. reported for the first time the photocatalytic antibacterial effect of TiO_2 (Matsunaga, Tomoda et al. 1985). Since then, photocatalytic disinfection has become a research focus of TiO_2 photocatalysis, especially in the medical realm. The photocatalytic bactericidal effect of anatase has been thought to lie in the generation of active radicalic and anionic oxygen species during light illumination (Kikuchi, Sunada et al. 1997, Maness, Smolinski et al. 1999, Rupp, Haupt et al. 2010). These active groups could initiate the peroxidation reactions in bacterial plasma membranes and disrupt the cell structure (Joost, Juganson et al. 2015).

Sunada et al (Sunada et al. 2003) put forward a 3-step mechanism to explain the general process of photocatalytic antibacterial performance on TiO₂ surfaces (Figure 2): (1) Attack of the cell walls by ROS. During this stage the outer membrane of the cells can be partially damaged and thus lead to the change of the permeability of the bacteria. This creates some passages in the cell walls for the ROS to enter into the cells easily. (2) Disordering of the inner cytoplasmic membrane and killing of the cell. In this stage the cell membrane undergoes lipid peroxidation and the structural and functional disordering of the cytoplasmic membrane takes place. (3) Decomposition of the toxic ingredients of bacteria. After longer reaction times, the dead bacteria are completely mineralized to CO₂ and H₂O.

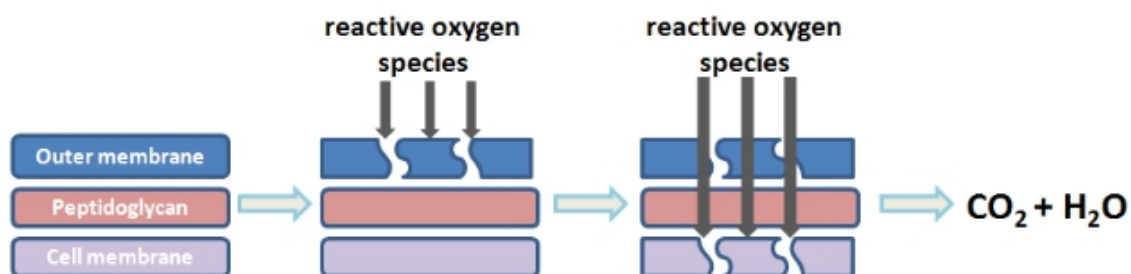


Figure 2: The three-step mechanism of photocatalytic bactericidal process on irradiated TiO₂ surfaces.

*This figure was modified from Fig.3 in publication *Visai et al. 2011*

1.4 Quartz crystal microbalance with dissipation

In this study, a quartz crystal microbalance with dissipation (QCM-D) device was used to detect the loading situation of bacteria on anatase surface.

The QCM-D is a nanogram sensitive technique that utilizes acoustic waves generated by oscillating a piezoelectric, single crystal quartz plate to measure surface mass and also characterize viscoelastic properties of bound masses via energy dissipation measurements.

The basis of QCM-D lies in the piezoelectricity, i.e., by applying alternating current to the quartz crystal an alternating expansion and contraction of the crystal lattice is induced. Normally, the shear quartz crystal is sandwiched between two metal electrodes, and the resonance would be excited when a sufficient AC voltage is applied with a frequency close to the resonant frequency of the crystal.

QCM-D is a popular technique to study the adsorption kinetics and mechanical properties of thin molecular films at the solid-liquid interface (Macakova 2010). In general, the amount of adhering mass on the oscillating quartz crystal is shown by the shifts in resonance frequency. What's more, when the adsorbed mass is viscous and sufficiently soft which doesn't follow the sensor oscillation perfectly (e.g., in the cell adsorption), this leads to internal friction in the adlayer and energy dissipation. Therefore, in biomolecular studies, QCM-D offers the ability to monitor viscoelastic film adsorption (e.g. proteins, DNA, lipids and cells) on different types of surfaces, by means of online measurements of resonant frequency and dissipation factor (Dixon 2007, Olsson 2011).

1.5 Aim of the study

Although a wide range of bacteria, fungi, algae and viruses were observed to be killed on UV-responsive TiO₂, there is a big drawback of this approach when intended to be applied in clinical situations. There, the high energy of UV irradiation might be harmful for living tissues and cells, thus limiting this antimicrobial approach to in vitro applications. Therefore, for specific applications, e.g., for peri-implantitis treatments adjacent to host tissues, it is important to clarify if the photocatalytic antimicrobial effects can also be excited in the visible (VIS) light region instead higher energetic UV.

In a previous study, we have reported about photocatalytic protein decomposition on anatase surfaces (Wu et al. 2015). It was found that pre-adsorbed human serum albumin (HSA) thin films could be photocatalytically decomposed not only in the usually applied UV-A range, but also under > 390 nm light irradiation, which lay in the transition region between UV-A and visible light, and this wavelength range was more clinically acceptable. Since proteins are basic components in the structure of bacteria, it can be supposed that bacteria may also get photocatalytically decomposed when irradiated by this clinically more acceptable light. Therefore, the idea for the present study was to investigate if light emitted at UV/VIS threshold wavelengths would be able to initiate a bactericidal attack on a pre-adhered early oral colonizer. In order to simulate the clinical oral situation in this in vitro study, human salivary pellicle films served as conditioning intermediate films at the implant/bacteria interface. In detail, the aims of this study were as follows:

- 1) To detect online changes of bacterial attachment on anatase surface in different irradiation situations in a model system (QCM);
- 2) To observe qualitatively the photocatalytic antibacterial effects of anatase in different irradiation situations by Live/Dead staining and microscopic examination;
- 3) To quantitatively determine the photocatalytic antibacterial effects of anatase in different irradiation situations by analyzing the microscopic images.

2. Materials and methods

2.1 Preparation of samples

AT-cut 5-MHz quartz crystals (14 × 0.3 mm, Q-Sense, Sweden) served as the substrates for anatase coatings. The polycrystalline anatase layers with a thickness of 700 nm were prepared by reactive pulse magnetron sputtering at Fraunhofer Institute for Organic Electronics, Electron Beam and Plasma Technology (FEP, Dresden, Germany) (Figure 3). The reactive pulse coating technique has been investigated for the past few years and the phase of growing films can be tailored to a large extent by choosing proper process conditions and pulse parameters (Zywitzki, Modes et al. 2004, Frach, Glöß et al. 2006). Ultrapure and nanostructured layers of anatase could be produced by this technique (Rupp, Haupt et al. 2010).

The procedure of reactive pulse magnetron sputtering was like this: after charging and evacuation of the deposition chamber, the substrates were preheated in vacuum to a temperature of 200 °C and exposed to a short plasma-etching process to support layer adhesion. Subsequently, anatase layers were deposited in a reactive magnetron-sputtering process in bipolar

pulse mode with a frequency of 20 kHz. The reactive working point of the process was stabilized by a closed-loop feedback control on the optical plasma emission signal in a region where fully transparent, stoichiometric TiO₂ films grow on the substrates. The working pressure was kept at 1 Pa for these depositions and the process conditions have been reproduced in several deposition runs for a multitude of coatings. A duration of deposition between 9 and 15 min was chosen to account for the different substrate geometries and movements during deposition. After the deposition, substrates were allowed to cool down to 100 °C before venting of the chamber for decharging (Rupp, Haupt et al. 2010).

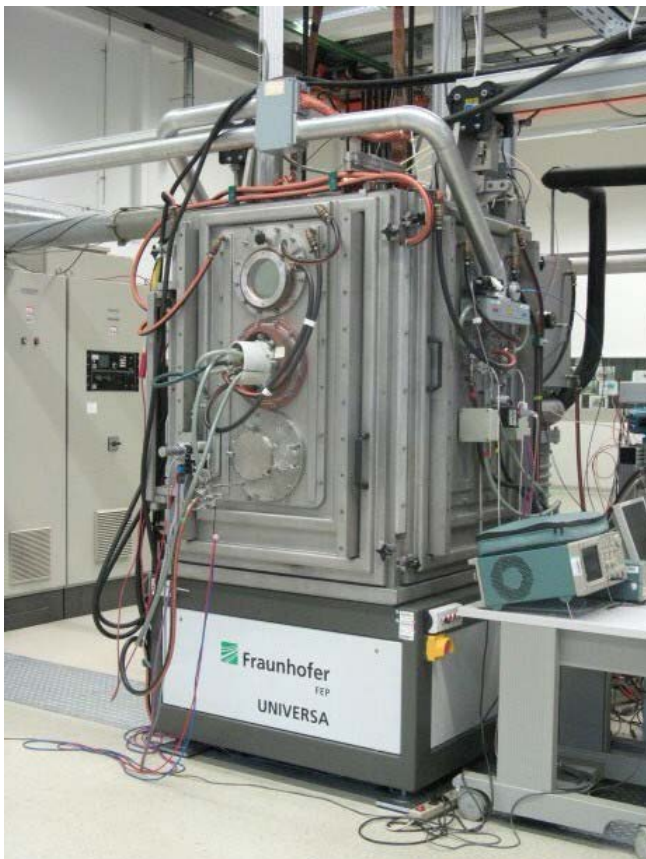


Figure 3: The reactive pulse magnetron-sputtering machine for anatase coating.

In this study, beside the anatase-coated quartz crystals, Ti-coated quartz crystals were also utilized as reference surfaces.

2.2 Surface Characterization

The polycrystalline morphology of the anatase films was scanned by electron microscopy (Ultra high-resolution field-emission SEM; SU8000, Hitachi High-Technologies, Krefeld, Germany). A fracture of the film was produced by a deep scratch and cross-sections of the films were observed along the exposed edges.

2.3 Human sterile saliva

After collecting the human whole saliva from one healthy volunteer in sterile 50-mL polypropylene falcon tubes, the saliva was filtered through a 70 µm cell strainer (BD Falcon, BD Biosciences, Durham, USA), centrifuged at 4 °C and 14,000 g for 30 min, and finally sterile-filtered by subsequent use of 5 µm (repeat 2 times) and 0.45 µm (repeat 10 times) low protein binding syringe filters (Acrodisc Syringe Filters with Supor PES membrane; Pall, Cornwall, UK). The filtrates obtained were diluted 1:5 with phosphate-buffered saline (PBS; DPBS, Gibco®, life technologies, Germany) and stored at -18 °C. After thawing and sonicating for homogenization, the saliva samples were used without further treatments for the experiments.

2.4 Bacteria suspension

In this study, *Streptococcus gordonii* (*S. gordonii*), which is a member of viridians streptococci, was chosen as model bacterium.

In the process of oral biofilm formation, *S. gordonii* serves as a pioneer organism and plays an integral role in initiating colonization by creating

adhesion sites for other colonizers (Plummer and Douglas 2006). In this study, the *S. gordonii* strain DL1 originated from S. Ruhl (Department of Oral Biology, State University of New York at Buffalo, USA) was utilized. After growing as stationary suspension culture in Schaedler medium (Beckton Dickinson GmbH, Germany) at 37 °C for 18 h, bacteria deposit was harvested by centrifugation for 5 min at 170 g and discarding the supernatant liquid. Then, the bacteria deposit was resuspended in PBS and further diluted until an optical density (OD) of 0.54 was reached, indicating a final bacterial concentration of 1×10^8 ml⁻¹. To measure the OD value, 200 µl bacteria suspension was loaded in one well of a 96-well plate and the plate was laid into the detect chamber of an ELISA immunosorbent device (SLT, Germany), the OD value was measured at a wavelength of 620 nm and recorded by the BIOLISE software.

2.5 Protocols of light irradiation

To seek for possible photocatalytic effects under different light regimes, several irradiation conditions (Bluepoint, Hoenle, Germany) have been established:

- A. UV-A, Mercury lamp > 320nm, with 365 nm peak wavelength, 25 mW cm⁻², 3 min (bluepoint 2 easycure, Hoenle, Germany)
- B. UV-A/VIS, LED > 380nm, with 405 nm peak wavelength, 1050 mW cm⁻², 10 min, (bluepoint LED, Hoenle, Germany)
- C. UV-A/VIS, LED same as B, 1050 mW cm⁻², an additional 390 nm cutoff-filter (LongPass Color Filter, THORLABS, Germany) was placed under the light source to exclude wavelengths below 390 nm, 10 min.

D. VIS, LED same as B, 1050 mW cm^{-2} , an additional 405/10 nm band-pass filter (BandPass Color Filter, ahf, Germany) was placed in the light path to limit the irradiation to 400-410 nm, 10 min.

The radiant exitance (UVA 25 mW cm^{-2} ; UV-A/VIS 1050 mW cm^{-2}) utilized in this study was fixed according to the previous reports (Rupp et al. 2010, Rupp et al. 2012) and some pilot studies, which was proved to be able to induce the photocatalytic decomposition of organics.

Up till now, the threshold between UV-A and VIS wavelength range is not yet clearly defined. On the one hand, the VIS range has been defined by wavelengths from 380-780 nm (Asahi et al. 2001); on the other hand, a VIS range of 400-780 nm has been reported (Wang et al. 2014). Accordingly, UV-A ranges from 315 nm till 380 or 400 nm, dependent on the literature. Due to this imprecisely defined UV-A/VIS threshold value, we defined in our study the wavelength range $380 \text{ nm} < \lambda < 400 \text{ nm}$ as UV-A/VIS threshold irradiation to consider this transition zone between UV-A and visible light.

2.6 QCM tests

The quartz-crystal microbalance device (QCM-D; D-300, Q-Sense, Sweden) was used for the QCM tests (Figure 4). This online system consists of 3 main parts: electronics unit for monitoring the experimental conditions, a flow cell for loading the acoustic sensors, and Q-Sense Software for recording the frequency (f) and dissipation (D) signals of the quartz oscillation. Since in this study the saliva and bacteria suspension was needed to be driven across the sensor surface at a certain speed, the peristaltic pump (ISMATEC, Germany) was used to control the flow rate.

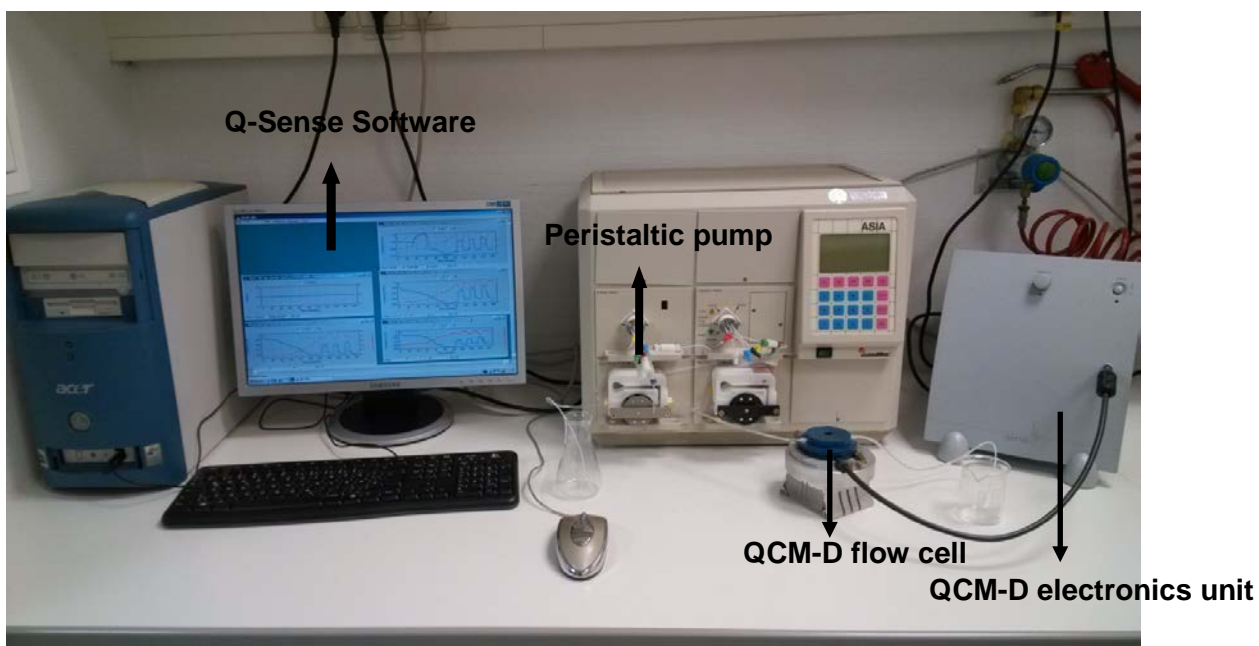


Figure 4: The equipment setting of the QCM-tests.

Anatase-coated AT-cut piezoelectric quartz crystal sensors of 14 mm diameter (Q-Sense, Sweden) (Figure 5) were sandwiched between gold electrodes that provide an electrical connection via pins in the flow cell to the electronics unit (Figure 6).



Figure 5: Both sides of the quartz-crystal.

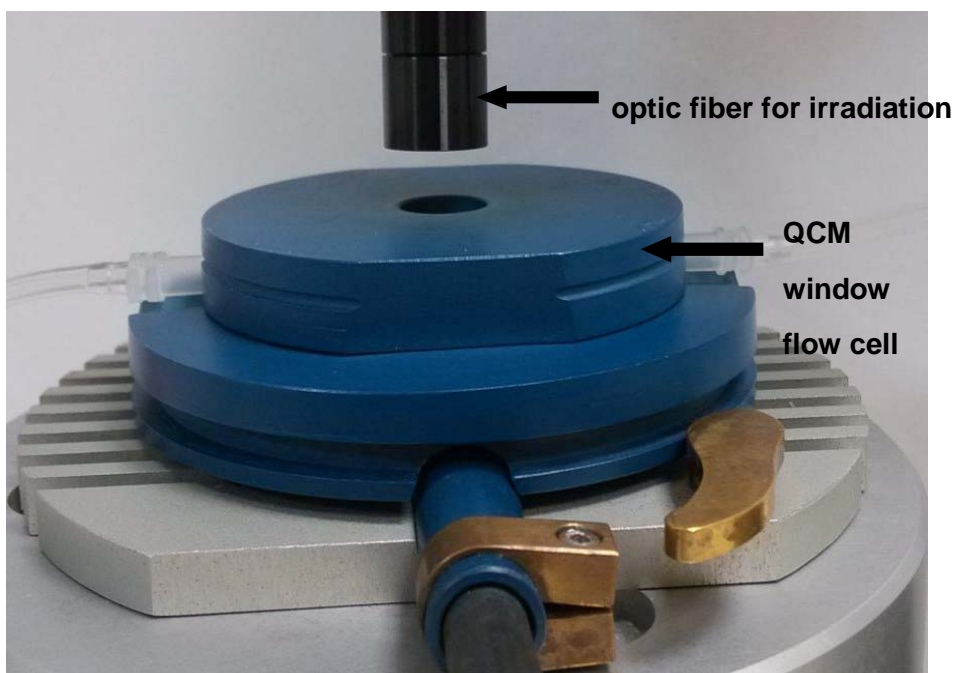


Figure 6: The combination of light irradiation and QCM-D. The window flow cell is part of QCM equipment, as shown in Figure 4.

These sensors were excited to oscillate by applying an alternating current across the electrodes at its fundamental resonant frequency (5 MHz), and at the 3rd, 5th and 7th overtones (Ash, Mulholland et al. 2014). Based on piezoelectricity, the applied voltage would lead to resonance of the crystal and results in an evanescent wave extending into the adjacent medium. In QCM measurements, the Sauerbrey equation (Equation 1) is the theoretical basis to analyze changes in the adsorbed mass by frequency changes (Sauerbrey 1959).

$$\Delta m = -\frac{C}{n} \Delta f \quad (1)$$

in which C is the mass sensitivity constant ($C = 17.7 \text{ ng cm}^{-2} \text{ Hz}^{-1}$ at 5 MHz) and n is the frequency overtone number (1, 3, 5, 7) (Jordan and Fernandez 2008). The lowest value of hydrated pellicle mass could be estimated through

this method, while other models might overestimate the amount of pellicle adhesives (Ash et al. 2014). According to the Sauerbrey equation, a decrease in the resonant frequency (Δf) is proportional to mass deposition (Δm). However, if the adsorbed film develops visco-elastic properties, such as often observed during bio-macromolecular or bacterial interactions, the amplitude of oscillation is also influenced by dissipative energy losses of the adsorbed film and in this case the dissipation should be taken into consideration to evaluate the adsorbed mass (Vogt et al. 2004):

$$D = \frac{E_{Dissipated}}{2\pi E_{Stored}} \quad (2)$$

In which $E_{dissipated}$ refers to the energy dissipated during one oscillatory cycle and E_{stored} indicates the energy stored in the oscillating system.

After all, biomaterial/biosystem interactions can be observed in real-time from the acquired frequency and dissipation signals if the sensor is integrated in flow-systems.

In our experiments, the anatase-coated quartz crystals were placed into a window flow cell (QS-QWIC 301 Q-Sense, Sweden) to form the base of the flow chamber. Stable signal baselines under PBS rinsing at a basic injected flow rate of $110 \mu\text{l min}^{-1}$ were defined as a prerequisite to start the experiment. Then, the saliva solutions were pumped over the quartz surface for 30 min, followed by a 30 min PBS rinsing step. Subsequently, the *S.gordonii* suspension was perfused through the flow cell for 10 min, followed by a 30 min PBS rinsing step to remove loosely attached bacteria. After salivary

conditioning and bacterial interaction, the sensor surfaces were irradiated by the respective light fiber (UV-A, VIS) from top, meanwhile, the PBS rinsing continued and its flow rate was modified according to one of the following four schemes:

- 1) The light irradiation was combined with increased PBS flow rate ($2700 \mu\text{l min}^{-1}$). The irradiation was repeated 3 times according to the conditions in section *Protocols of light irradiation*, with an intermediate break interval of 15 min without irradiation and a basic flow rate ($110 \mu\text{l min}^{-1}$).
- 2) Reference test I: this test was conducted without irradiation, but with the increased flow rate ($2700 \mu\text{l min}^{-1}$), i.e., 3 times of 10 min rinsing with increased flow rate ($2700 \mu\text{l min}^{-1}$) and with 15 min intermediate interval at a basic flow rate ($110 \mu\text{l min}^{-1}$).
- 3) Reference test II: this test was conducted with UV-A/VIS, LED > 380 nm irradiation, but at the basic flow rate ($110 \mu\text{l min}^{-1}$). The irradiation was also repeated for 3 times of 10 min, with 15 min intermediate interval.
- 4) Reference test III: this test was conducted by using Ti-coated quartz crystals combined with UV-A irradiation, also with the increased flow rate ($2700 \mu\text{l min}^{-1}$). The irradiation was repeated 3 times for 3 min, also with 15 min intermediate interval at a basic flow rate ($110 \mu\text{l min}^{-1}$).

2.7 Hydrodynamic Calculations

It has been reported that when fluid flow exceeds a critical limit, the resulting wall shear rates may become high enough to stimulate microbial detachment from surfaces (Christersson et al. 1988). The purpose of the study was to focus on the antibacterial performance of photocatalytic effects; however, the

flow rate of solution might be an interfering factor since it might also induce microbial detachment. Therefore, in the experimental protocol, the flow rate of injected PBS was modulated between a higher (2700 $\mu\text{l min}^{-1}$) and the basic (110 $\mu\text{l min}^{-1}$) value and the reference tests I and II were designed, as described in Chapter 2.6. Through this design, the respective influence of irradiation and flow rinsing on antibacterial effects could be observed and analyzed.

In addition, to analyze a possible antibacterial effect induced by rinsing at an increased flow rate, the hydrodynamic situation in the QCM-D flow cell was evaluated.

Based on the report by Vanoyan N (Vanoyan et al. 2010), since the fluid velocities differed at varied locations in the flow cell, the shear stress profile G_{sh} in the QCM-D could be calculated according to the equation:

$$G_{sh} = \frac{3V_m}{b^2} (b - z) \quad (4)$$

V_m is the mean fluid velocity, b is half the flow cell height and z is the distance coordinate perpendicular to the surface ($z=b$ in the middle of the flow cell and $z=0$ at the surface). V_m was estimated according to the average cross-sectional area, which was assumed by dividing the maximum cross-sectional area by 2, in this study, the height of the circular flow cell was 0.50 cm and the diameter was 1.08 cm, so the maximum cross-sectional area would be 0.54 cm^2 and the average area would be 0.27 cm^2 . Based on this average area value, V_m was calculated to be 0.0068 cm s^{-1} and 0.17 cm s^{-1} with the injected

flow rate at $110 \mu\text{l min}^{-1}$ and $2700 \mu\text{l min}^{-1}$, respectively. The highest shear stress in the flow cell would be near the surface and in this study, the maximum shear rate G_{sh} value would be 0.0816 s^{-1} and 2.04 s^{-1} with the injected flow rate at $110 \mu\text{l min}^{-1}$ and $2700 \mu\text{l min}^{-1}$, respectively.

2.8 Live/Dead staining and microscopic examination

A Molecular Probes LIVE/DEAD® BacLight™ Bacterial Viability Kit (catalog number: L-7007, Molecular Probes, Life Technologies GmbH, Germany) was used. The LIVE/DEAD® BacLight™ Bacterial Viability Kits utilizes two kinds of dyes, i.e., SYTO® 9 green-fluorescent nucleic acid stain and the red-fluorescent nucleic acid stain, propidium iodide.

These stains differ in their spectral characteristics and in their ability to penetrate healthy bacterial cells. When used alone, the SYTO® 9 stain generally labels all bacteria in a population — those with intact membranes or with damaged membranes. In contrast, propidium iodide penetrates only bacteria with damaged membranes, causing a reduction in the SYTO® 9 stain fluorescence when both dyes are present. Thus, with an appropriate mixture of the SYTO 9 and propidium iodide stains, bacteria with intact cell membranes are stained fluorescent green, whereas bacteria with damaged membranes are stained fluorescent red.

In this kit, both dyes exist in the form of powder and are respectively stored in the plastic pipettes. To prepare the dye solution, 2.5 ml distilled water (Ampuwa®, Fresenius Kabi France) was first transferred into a dish, then the pipette was cut open and the distilled water was drawn into and drained out of the pipette repeatedly. When all the powder dissolved, the dye solution in the dish was distributed into eppendorf tubes (Eppendorf AG, Hamburg, Germany),

and each tube was loaded with 100 μ l dye solution. The eppendorf tubes loaded with dye solution were stored at -20 °C in darkness. Before staining, the eppendorf tubes were brought out from the freezer and thawed, then, the mixture of the dye solution was prepared, that is, 1 ml distilled water + 100 μ l SYTO 9 solution + 100 μ l Propidium iodide solution. The excitation/emission maxima for these dyes are about 480/500 nm for SYTO 9 stain and 490/635 nm for propidium iodide. The background remains virtually nonfluorescent.

After the QCM tests, the quartz sensors were demounted from the flow cell and immersed in the dye mixture for 15 min. Then the quartz crystals were rinsed with water to get rid of the redundant dye solution. The samples were examined with a fluorescence microscope (Optiphot-2, Nikon) equipped with a remote control DSLR (Nikon 550D). To visualize the organisms, a filter combination with 450-490 nm excitation bandpass and a 520 nm highpass emission filter (Nikon B2 Filtercube) were used.

2.9 Image analysis

From the fluorescent microscopic images, the red- (indicating the dead bacteria) and green- (indicating the live bacteria) colored regions on the images were selected and the corresponding pixels were calculated by GIMP software (Gimp 2.8, General Image Manipulation Program, The GIMP Development Team, USA). First, the pixel numbers of the fluorescent red and green areas were calculated respectively. Then, the pixel proportion of dead bacteria was calculated by dividing the pixel numbers of red areas by the sum of the pixel numbers of red and green areas. By calculating the pixel proportion of dead bacteria in the whole colored region, the respective antibacterial effects could be compared.

2.10 Statistical analysis

The QCM experiments were repeated at least three times for each irradiation or reference case and typical frequency and dissipation curves are exemplarily shown in the results section. For each QCM run, three representative fluorescent images were chosen for the statistical analysis, and the pixel proportions were expressed as means with standard deviations. Differences among means of these data were statistically analyzed by one-way analysis of variance (ANOVA) followed by Student-Newman-Keuls (SNK) test. Differences were regarded as statistically significant when $P < 0.05$ (SPSS 17.0, IBM, USA).

3. Results

3.1 Surface properties

Figure 7 shows the scanning electron microscopy image of the cross-section of the polycrystalline anatase films on Ti-precoated quartz crystals. The films showed a column structure and pronounced faceted faces at the surface, with 100 -200 nm lateral size at the top surface. In growth direction, the crystallites extended over nearly the entire film thickness. The Ti basis appeared as a bright layer at the substrate interface. On top of that, anatase growth began with a relatively small lateral scale length, which then coarsens by competitive growth of individual crystallites.

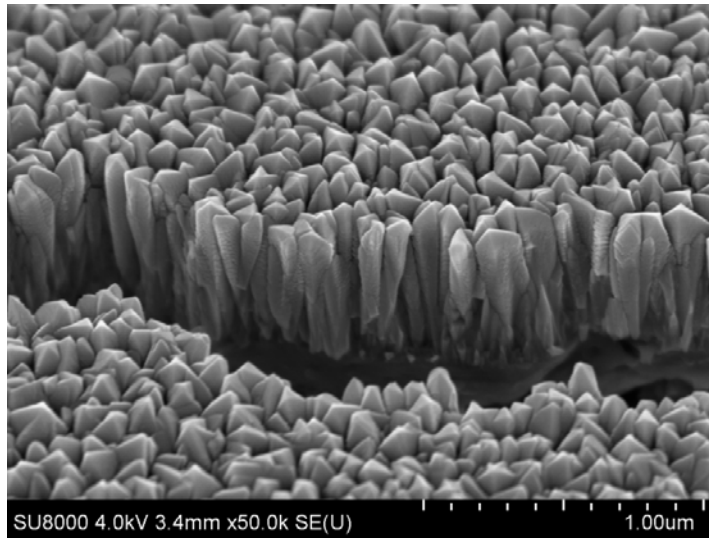


Figure 7: SEM image of the fracture of anatase film on a Ti-coated quartz crystal ($\times 50,000$).

3.2 QCM online experiments

During the QCM experimental runs, frequency and dissipation were recorded in real-time, and the signal development at the 7th overtone for frequency and dissipation are exemplarily shown in Figures 8a-g. The standard noises of the frequency and dissipation signals in PBS medium are < 1 Hz and < 0.06 E-6, respectively. The preconditioning of the sensor surfaces with saliva and the following loading of bacteria resulted in a frequency decrease and an increase in the dissipation signals. The frequency and dissipation shifts before and after 3 times of irradiation were summarized in Table 1. The baseline value of frequency (or dissipation) before infusing saliva were defined as F1 (or D1), and the stable levels acquired just before irradiation were defined as F2 (or D2). Likewise, the stable levels acquired after irradiation procedure were defined as F3 (or D3) (Figure 7a). ΔF (or ΔD) before and after irradiation were calculated by F2-F1 (or D2-D1) and F3-F1 (or D3-D1), respectively. The frequency (or dissipation) reversion described the reversion extent of

frequency (or dissipation) signals to the baseline level, after 3 times of irradiation. When the value of reversion had a positive sign, this indicated that the signals moved in the direction towards the baseline; In contrast, a negative sign indicated that the signals moved in the opposite direction away from the baseline.

In case of irradiation with UV-A source (Figure 8a), the frequency level rose sharply to the baseline after the first irradiation and remained at this level for another two irradiations reaching an average reversion of 91% after 3 times of irradiation. Simultaneously, the dissipation signals descended gradually after each irradiation reaching eventually the initial dissipation baseline level.

Upon UV-A/VIS irradiation > 380 nm (Figure 8b), the frequency shifts were very similar to that observed upon UV-A. Also here, the frequency quickly rose after the first irradiation and finally reached an average reversion of 87%. However, in contrast to the effects of UV-A, there was no explicit change of dissipation signals. A partly-reversion shift was shown in Figure 8b, while in several other replicate tests the dissipation signals showed a rising tendency, so the mean dissipation reversion was negative (-13 %).

A different behavior in the frequency development was observed at longer irradiation wavelength. Figure 8c showed the results when applying wavelengths > 390 nm. Here, the frequency signal rose step by step and a mean value of 68 % reversion to the baseline could be observed after the third irradiation. Likewise, the dissipation development differed from that observed under UV-A irradiation, that is, the dissipation values increased stepwise after each irradiation and the mean dissipation reversion reached finally -94 %.

Finally, when limiting the irradiation to wavelengths between 400 and 410 nm, a stepwise increase of the frequency signals to a mean value of 88 % reversion after the third irradiation appeared. Figure 8d showed an example of 100 % reversion. Besides, no apparent changes occurred in the dissipation when irradiation wavelengths < 400 nm were now excluded.

In the reference tests I, which were conducted without irradiation, no obvious changes of frequency and dissipation signals could be observed (Figure 8e).

In the reference tests II, the bacterial films were irradiated with UV-A/VIS, LED > 380 nm, but the runs were conducted with the basic flow rate. Although it seemed here that the frequency signals didn't reach the baseline level directly after the first irradiation, a complete frequency reversion could also be attained after the following irradiation (97%). The dissipation signals showed here an increase after the first irradiation and didn't return to the basic level at the end (Figure 8f).

In the reference tests III (Figure 8g), which were conducted on titanium surface, the gradual reversion of frequency signals was also observed after UV-A irradiation and reached a mean value of 64.5 % after the third irradiation. What's more, the dissipation signals did not show any reversibility but increased in course of three irradiations.

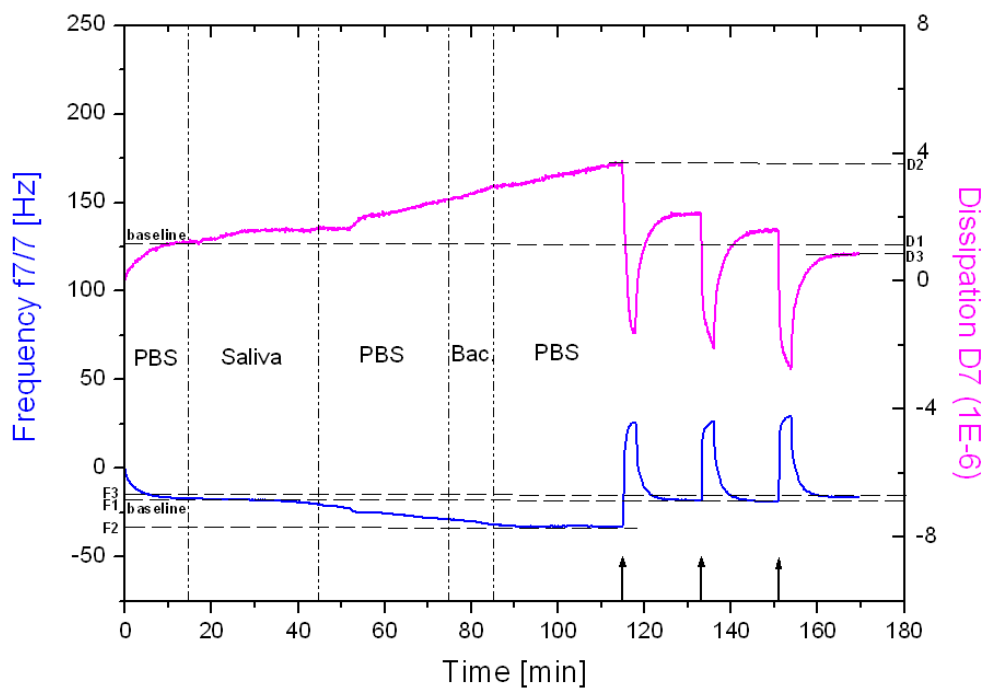


Figure 8a UV-A (> 320 nm), with higher flow rate ($2700 \mu\text{l min}^{-1}$) rinsing

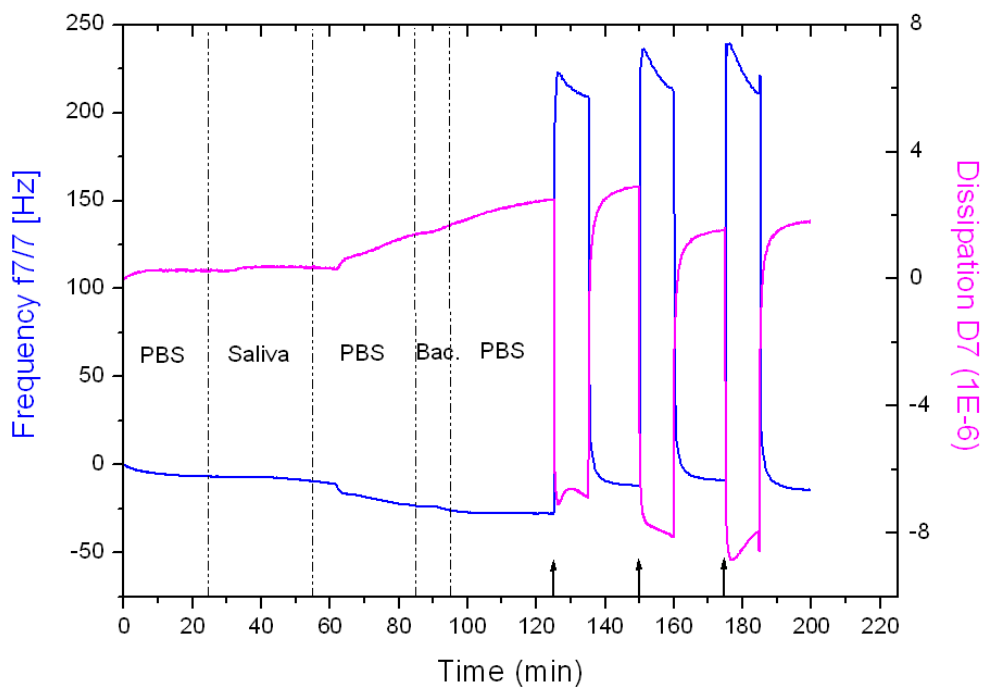


Figure 8b VIS (> 380 nm), with higher flow rate ($2700 \mu\text{l min}^{-1}$) rinsing

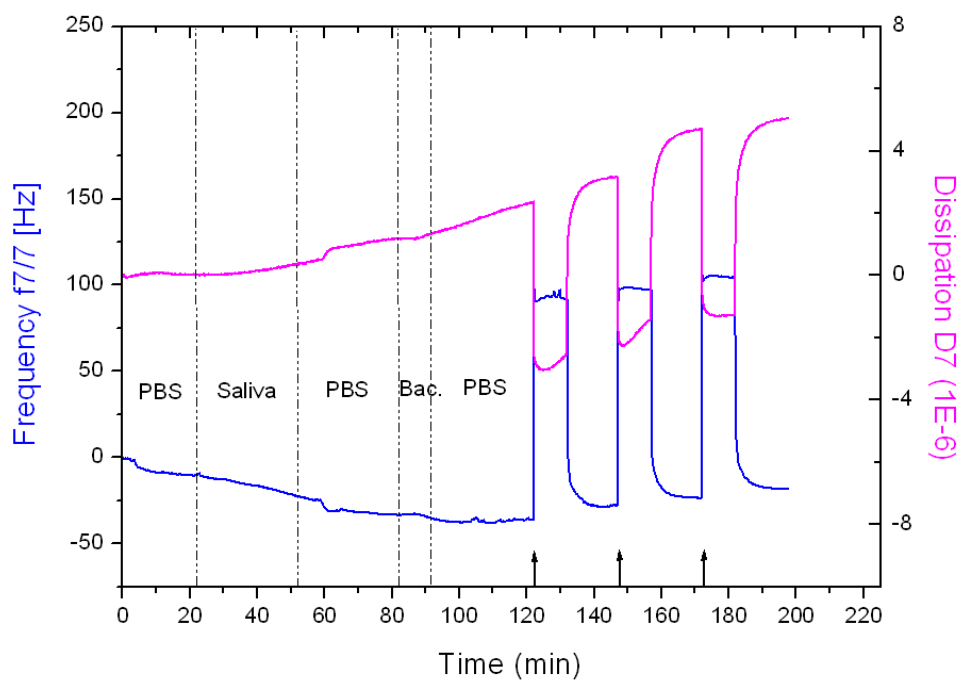


Figure 8c VIS (> 390 nm), with higher flow rate ($2700 \mu\text{l min}^{-1}$) rinsing

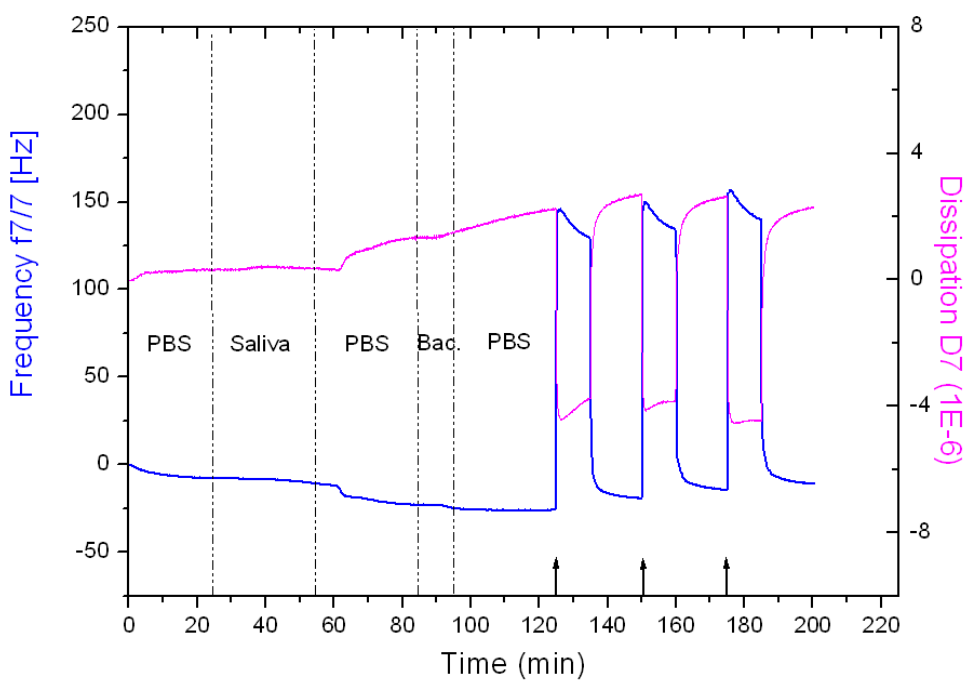


Figure 8d VIS (400-410 nm), with higher flow rate ($2700 \mu\text{l min}^{-1}$) rinsing

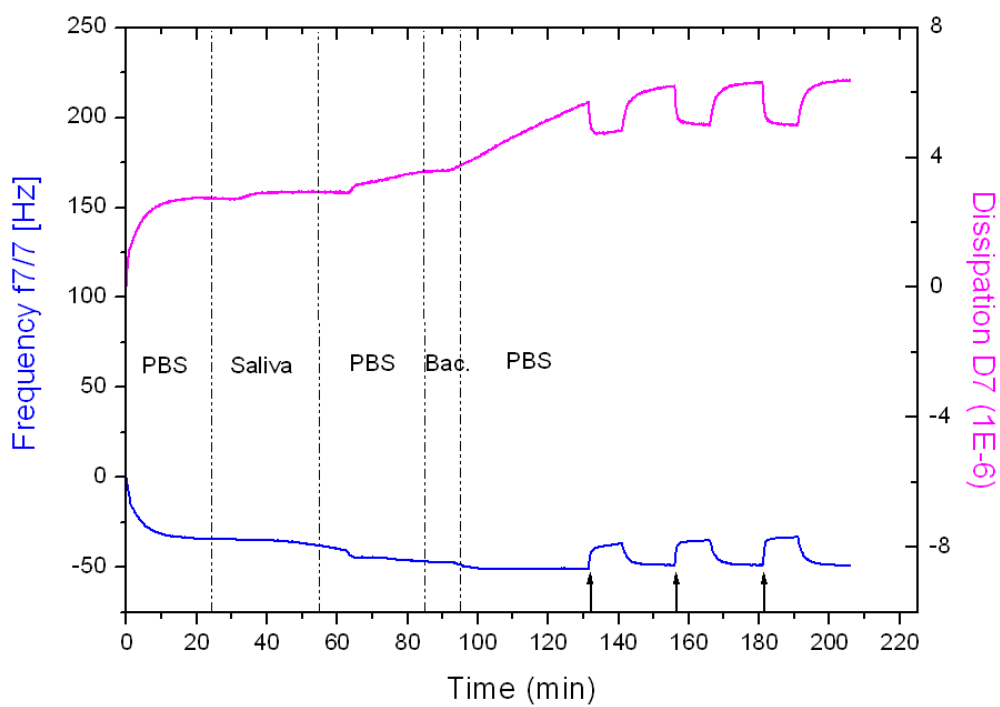


Figure 8e no irradiation, with higher flow rate ($2700 \mu\text{l min}^{-1}$) rinsing

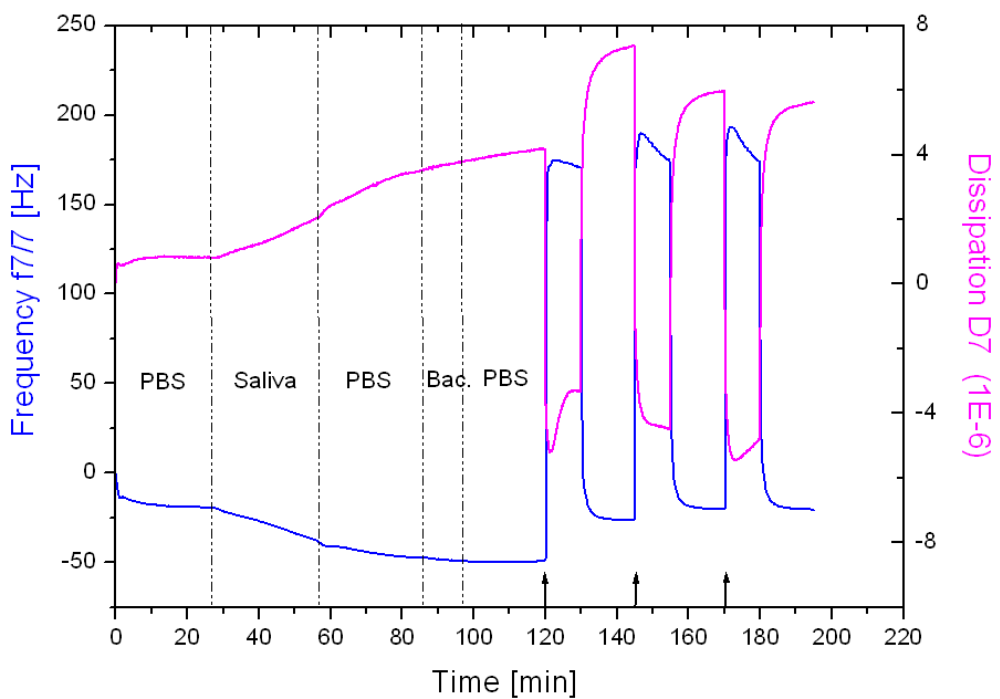


Figure 8f VIS ($> 380 \text{ nm}$) irradiation, with basic flow rate ($110 \mu\text{l min}^{-1}$) rinsing

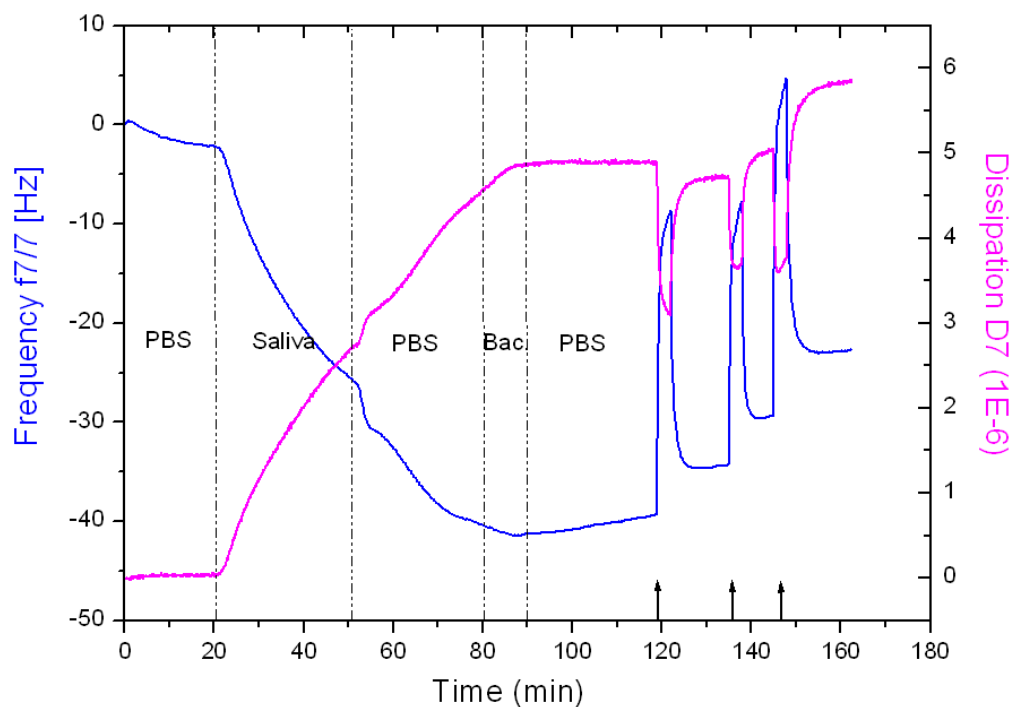


Figure 8g UV-A (> 320 nm) but on Ti surface, with higher flow rate (2700 $\mu\text{l min}^{-1}$) rinsing

Figures 8 a-g: Real-time QCM-D data under various irradiation protocols. (The arrows in Figures a-g indicate the start point of irradiation with or without flow rate change, and the arrows in e indicate the start point of flow rate change.) Figure a served as an example and was added with some indexes to show the reference levels to calculate ΔF (or ΔD).

Surface Material	Irradiation	$\Delta F_{7/7}$ (Hz)		Frequency Reversion (%)	ΔD (E-6)		Dissipation Reversion (%)
		Before irradiation	After irradiation		Before irradiation	After irradiation	
Anatase	UV-A (>320 nm)	-16 (1.4)	-1.5 (2.1)	91 (12.7)	2.2 (0.3)	-0.3 (0.1)	113 (4.2)
	VIS (> 380 nm)	-24 (4.6)	-3 (3.6)	86.7 (15.3)	2.2 (0.6)	2.5 (1.2)	-12.7 (37.8)
	VIS (> 390 nm)	-26 (6)	-7.7 (2.5)	67.7 (17)	2.5 (0.4)	5.0 (1.8)	-94.3 (43.5)
	VIS (400-410 nm)	-20 (1)	-2.3 (3.2)	87.7 (17.2)	2.0 (0.1)	1.8 (0.5)	7.3 (15.4)
	no irradiation	-20 (8.7)	-18 (9.5)	11.7 (11.7)	2.6 (1.6)	2.6 (1.5)	-9.2 (11.8)
	VIS (> 380 nm) basic flow rate	-44 (18.5)	-1.7 (4.7)	96.7 (8.5)	4.6 (1.9)	3.2 (1.4)	20.3 (54.8)
Ti	UV-A (>320 nm)	-31 (8.5)	-14 (9.9)	64.5 (10.6)	4.3 (0.8)	5.5 (0.5)	-29.1 (13.2)

Table 1: The frequency and dissipation shifts before and after 3 times of irradiation.

3.3 Microscopic analysis after Live/Dead staining

In Figures 9a-g, the bacterial layers of the different experimental runs after live/dead staining are shown respectively. In the reference group I (Figure 9e), multilayers of *S. gordonii* could be observed and numerous vital bacteria (fluorescent green) covered nearly the complete sensor surface, with only a small proportion of dead cells (fluorescent red) scattering among live ones. In contrast, upon UV-A irradiation, the quantity of *S. gordonii* decreased in general and the bacterial layer became thinner. Dead bacteria constitute the greatest proportion here and only minute amount of live cells could be observed (Figure 9a).

After UV-A/VIS irradiation > 380 nm, the photocatalytic bactericidal activity was similar as observed upon UV-A irradiation: the amount of bacteria also considerably declined and the majority of the remaining ones appeared to be dead (Figure 9b).

No bactericidal effect could be microscopically verified when the irradiation wavelengths were limited to longer than 390 nm. Here, the bacterial layers remained dense and live cells dominated in the visual field (Figure 9c). The same was observed when the higher energetic wavelengths were restricted further by band-pass-filtering to 400-410 nm, with nearly no different appearance compared with the reference tests I without irradiation. Most of the surface areas were occupied here by living cells and dead bacteria were only scattered sporadically (Figure 9d and 9e).

In the reference tests II, the results seemed to be the same as what could be observed in the situations with UV-A irradiation or UV-A/VIS irradiation > 380 nm, the dead bacteria occupied the surfaces to a large extent and only a few live cells dispersed among them (Figure 9f).

In the reference tests III, in which Ti surface were utilized and irradiated under UV-A, the bacteria layers were also dense and the dead bacteria were hardly to be seen on the fluorescent images (Figure 9g).

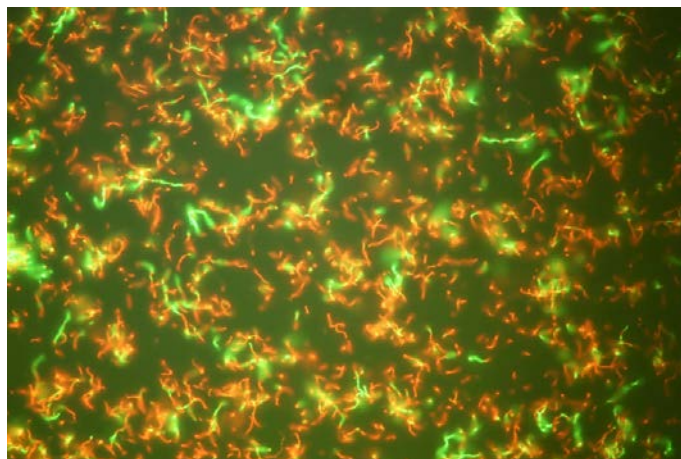


Figure 9a UV-A (> 320 nm), with higher flow rate (2700 µl min⁻¹) rinsing

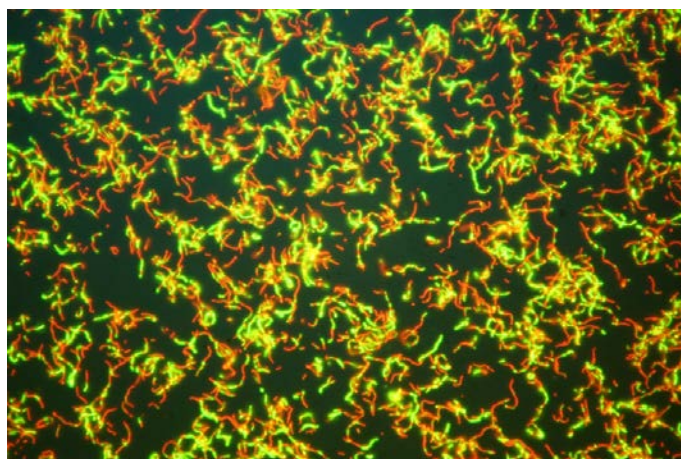


Figure 9b VIS (> 380 nm), with higher flow rate (2700 µl min⁻¹) rinsing



Figure 9c VIS (> 390 nm), with higher flow rate ($2700 \mu\text{l min}^{-1}$) rinsing

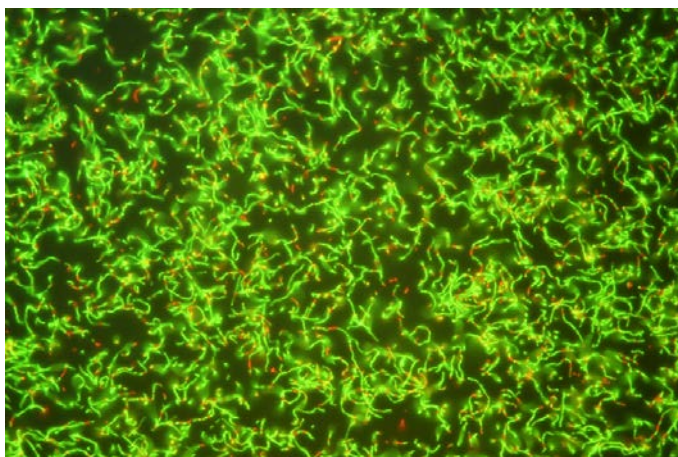


Figure 9d VIS (400-410 nm), with higher flow rate ($2700 \mu\text{l min}^{-1}$) rinsing

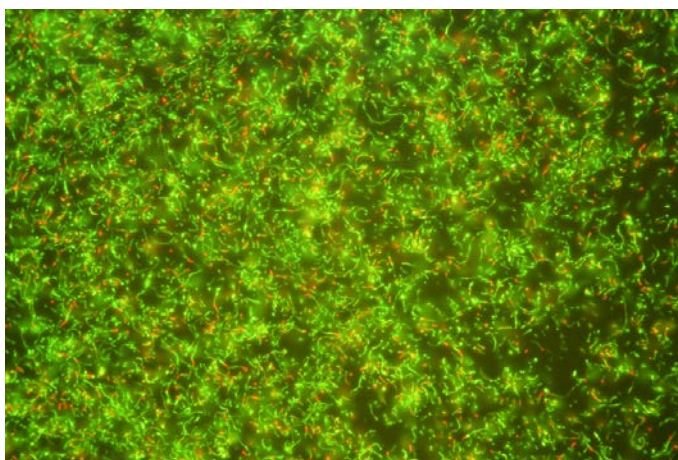


Figure 9e no irradiation, with higher flow rate ($2700 \mu\text{l min}^{-1}$) rinsing

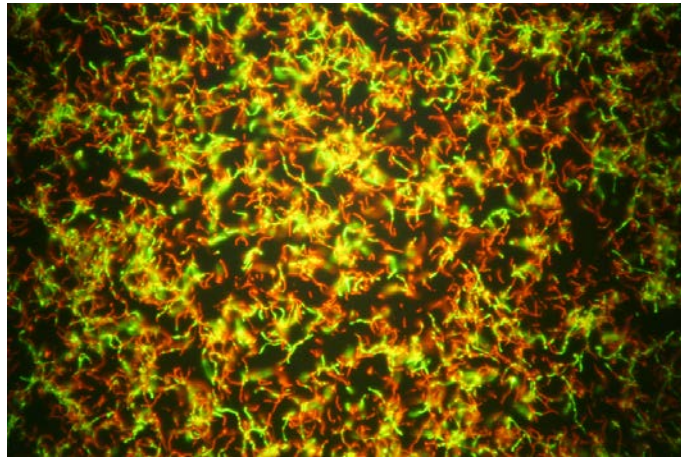
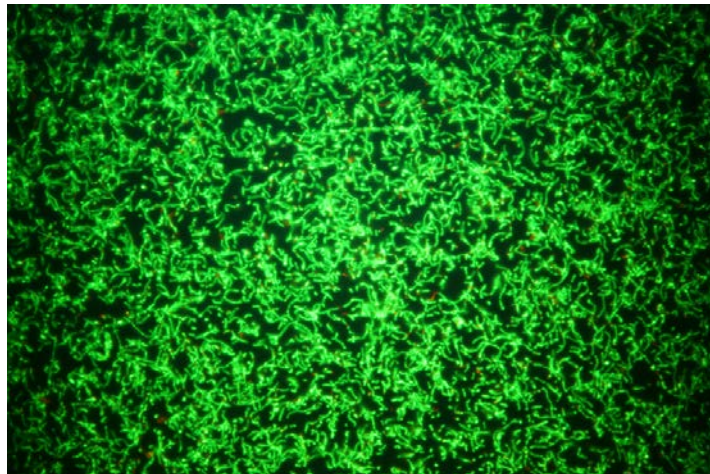


Figure 9f VIS (> 380 nm) irradiation, with basic flow rate ($110 \mu\text{l min}^{-1}$) rinsing



**Figure 9g UV-A (> 320 nm) but on Ti surface, with higher flow rate
($2700 \mu\text{l min}^{-1}$) rinsing**

Figures 9 a-g: Microscopic images after Live/Dead staining (400 \times).

3.4 Image evaluation

Figure 10 shows the results of the quantitative evaluation of images as shown in Figures 9a-g. Mean pixel proportions of regions with fluorescent red are shown for each irradiation situation. In the studies with increased rinsing flow rate

during irradiation ($2700 \mu\text{ l min}^{-1}$), significantly higher bactericidal effects were statistically proven under UV-A and UV-A/VIS $> 380 \text{ nm}$ irradiation compared to the other irradiation protocols ($P < 0.05$). There is no statistical significance between the mean values shown here for the UV-A and UV-A/VIS $> 380 \text{ nm}$ protocols ($P > 0.05$). What's more, the photocatalytic antibacterial effect under UV-A/VIS $> 380 \text{ nm}$ irradiation and with basic rinsing flow rate ($110 \mu\text{ l min}^{-1}$) showed also no significant difference in comparison with the results from UV-A and UV-A/VIS $> 380 \text{ nm}$ irradiation conducted at an increased flow rate ($P > 0.05$). On Ti surface, the fluorescent red cells only occupied 0.12% among the stained region, which is significantly lower than the other experimental situations ($P < 0.05$).

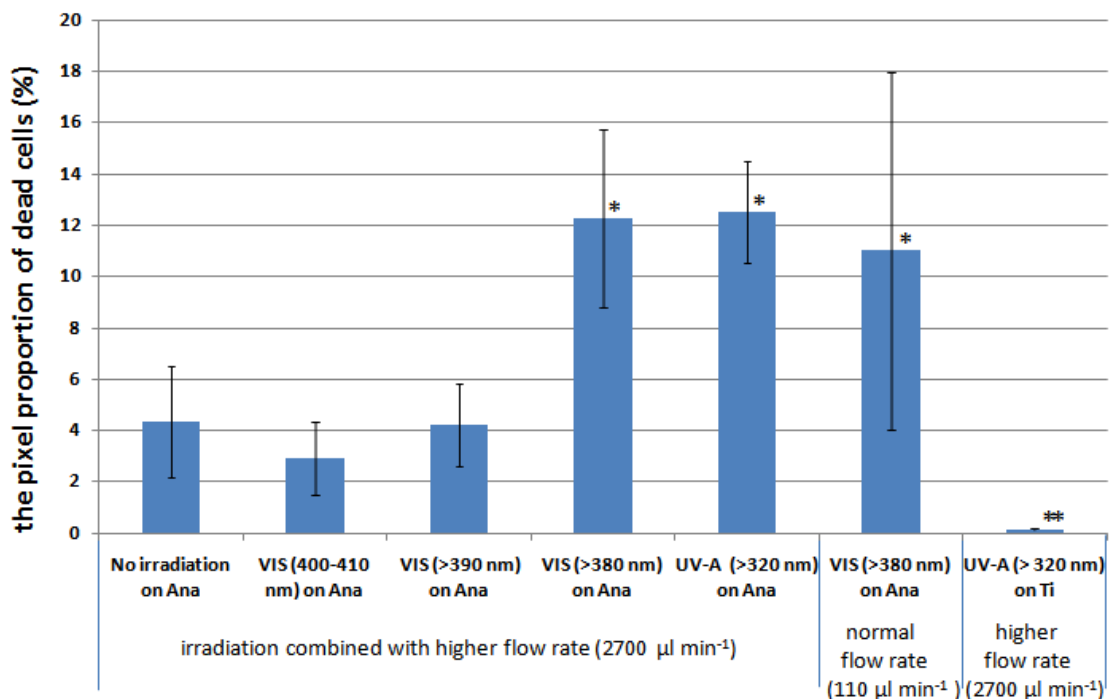


Figure 10: Pixel proportions of dead bacteria, calculated by dividing the pixels of red region (indicating dead cells) by the pixels of the whole colored region (red +

green, including dead and live cells). Each bar represented the mean proportion value from 9 analyzed images in the triplicate tests.

In Figure 10, the high standard deviation could be explained according to the discussion by other researchers, (Parmar et al. 2011, Yao et al. 2013), i.e., it might be resulted from the inhomogeneous distribution of living and dead bacteria in the bacterial layer and the subjective selection of the representative fluorescent images.

To sum up, in the present work, the salivary layer could be decomposed under each irradiation protocol, while the antibacterial effects could only be triggered upon UV-A or UV-A/VIS threshold illumination (> 380 nm). (Figure 11)

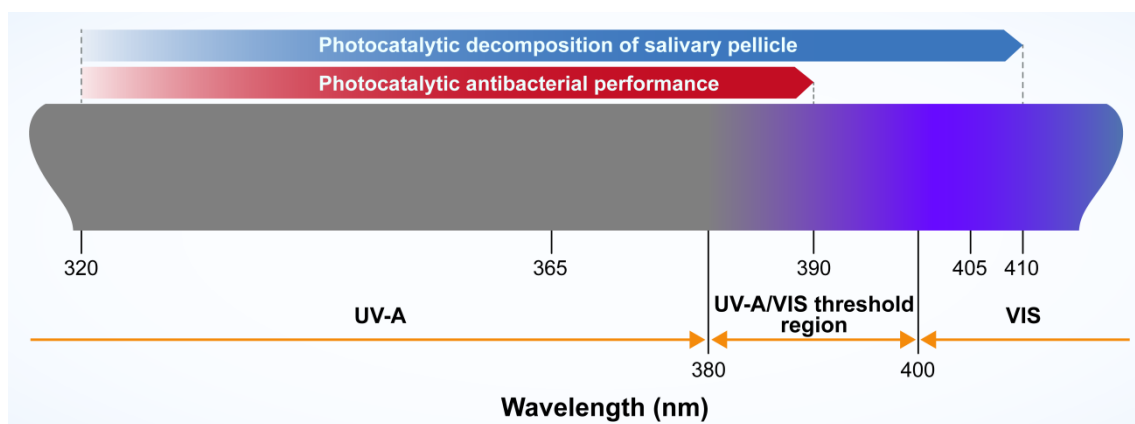


Figure 11: Effective spectrum region for inducing photocatalytic pellicle decomposition or antibacterial effects on anatase surfaces. In this study, photocatalytic antibacterial effects could be observed when the irradiation was < 390 nm; while the photocatalytic decomposition of salivary pellicle could take place even under 400-410 nm visible light irradiation.

4. Discussion

4.1 Analysis of the photocatalytic antibacterial performance

4.1.1 Analysis of the experimental results on Ti surface

Since the electronic state in pure metal is continuous, no band gaps exist between conductance and valence bands in Titanium (Jafari et al. 2012). As a result, there should be no photocatalytic effect shown on the pure titanium, even irradiated under UV light. In this study, only traces of dead bacteria could be observed in the fluorescent images after irradiating the Ti surface with UV-A and the pixel proportion of dead cells on Ti surface was significantly lower than any of other test situations (only 0.12 %). In comparison with the staining results in the other groups, it indicated that photocatalytic performance was material-related and no photocatalytic antibacterial effect could be observed on Ti surface.

However, when the QCM-D diagram was taken into consideration, some interesting phenomena could be noticed. In a previous study (Rupp et al. 2012), which dealt with the photocatalytic decomposition of salivary pellicle on anatase surface, Ti surface served as reference implant material and also received UV-A irradiation after conditioning with saliva pellicle. As the result, the frequency signals of Ti in the QCM-D experiments didn't show any visible rise even after UV-A irradiation, which indicated nearly no mass loss occurred on the surface and the attached pellicle film could hardly be photocatalytically decomposed on Ti surface. However, in this study, in the reference tests on Ti surface, frequency signals kept gradually rising after each UV-A irradiation and the dissipation signals also kept rising. Based on the principles of QCM-D, the

reversion of frequency indicated there was mass loss on the surface of quartz crystals and the rising of dissipation signals indicated the viscoelasticity of the adlayer was increasing, however, no obvious bacteria removal could be observed from the corresponding fluorescent images, which suggested the ascent of frequency curve here didn't simply display the change of adherent mass.

It has been pointed out in the literature, that bacterial adhesion cannot be totally explained by the conventional mass-loading theory. Bacteria like *S. gordonii* have filamentous structures and can excrete extracellular polymeric substances (EPS), which complicate the explanation of QCM results (Olsson et al. 2011, Krajewski et al. 2014). Up till now, there are still no specific reports aiming to figure out the relation between Frequency-Dissipation (F-D) signals in QCM and the photocatalytic antibacterial progress on the sensor surface. On the basis of the acquired results, it could be assumed that under UV-A irradiation some changes of the binding took place between the bacteria and the coated surface, which were independent of photocatalysis, e.g., the increasing viscoelasticity of the adlayer might be caused by local detachment of the filamentous connection, however, this needs more experiments to elaborate.

4.1.2 Analysis of the experimental results on anatase surface (irradiation with higher flow rate 2700 $\mu\text{l min}^{-1}$)

From the images of Live/Dead staining it was obvious that when the light wavelength was < 390 nm, the majority of bacteria on the anatase coating would be photocatalytically killed and get rid off from the surface. In contrast, when the irradiation wavelength was > 390 nm, the vitality of the bacteria seemed to be affected more faintly and the majority of bacteria still kept alive

and densely covered the surface. In combination with the appearance of F-D signals in QCM-D tests, more speculations could be produced regarding the condition of bacteria-substratum interface. In a pilot study, the photocatalytic decomposition of salivary pellicle, which formed on the anatase surface, was also investigated in QCM-D under different light irradiation. This pilot study showed that even under 400-410 nm light irradiation, > 60 % pellicle proteins could be decomposed. Based on this knowledge, it could be inferred that in all the irradiation cases in this study, the observed frequency reversions were partly attributed to the photocatalytic decomposition of salivary pellicle. And in the cases with wavelength < 390 nm, the loss of adhered mass caused by bacterial removal could also lead to frequency increase. In addition, the photocatalysis-independent frequency increase, which was shown in Ti reference tests, might also play a role in the frequency reversion on anatase surface.

Regarding the change of dissipation signals in different conditions, total reversion could always be observed after UV-A irradiation, which suggested a substantial loss of visco-elastic binding sites of the bacteria to the substrate. However, upon UV-A/VIS threshold irradiation, the dissipation shift became irregular and the signal either rose or changed little. Since the salivary pellicle should be photocatalytically decomposed in these situations, it could be hypothesized that the dead space at the anatase-pellicle interface formed by photocatalysis could serve as a breaking point for bacterial detachment; however, this hypothesis was not supported by the fluorescent staining results. Combined with the dissipation changes, it could be shown that the bacteria-surface interfacial connections were not disrupted and the binding sites might

be altered after the decomposition of salivary pellicle, thus increasing the viscoelasticity of the adlayer. After all, the photocatalytic antibacterial process appeared more complicated than the photocatalytic decomposition of protein layers; it might be influenced by a combination of factors, such as the property of the coating material, the connection situation of the bacteria-substratum interface, and the irradiation light.

Considering the sites on the bacteria where photocatalytic attack was observed, lipids and proteins in the cell membrane turned out to be the main targets in antibacterial photocatalytic treatment (Carré et al. 2014). The active oxygen species can initiate the peroxidation of fatty acids, which exist abundantly in bacterial plasma membranes, and cause their decomposition or structural changes. Consequently, the cell membranes were damaged and led to the leakage of cytoplasm (Joost et al. 2015).

Bacterial cells themselves have evolved some defensive methods to resist oxidative stress by radicalic oxygen species. Some self-produced enzymes such as catalase and superoxide dismutase can defend the microorganisms from fatal attack (Bonetta et al. 2013). On the other hand, since there is a thick peptidoglycan layer in the cell wall of Gram-positive bacteria, which might retard the diffusion of oxidants to the underlying phospholipid bilayers, Gram-negative bacteria (e.g. *E.coli*) are easier to be attacked under photo-illumination than the Gram-positive ones (e.g. *S. gordonii*) as a result of differences in cell wall or membrane structures (Gopal et al. 2004, Mitoraj et al. 2007). What's more, the penetration depth of generated oxygen species can be blocked by multiple bacterial layers and the limited lifetime of these reactive oxygen species might make it really hard to take effect inside the bacterial layer (Cai et al. 2014).

It is worthy to note that the photocatalytic antibacterial effects are also influenced by the material surface which serves as the photocatalyst. For example, the microtopography can also have some influence on photocatalytic antifouling effects (Ramya et al. 2010, Vucko et al. 2013). Smaller particle size and increased homogeneity of the surface are supposed to inhibit biofilm formation and allow more effective biofilm control.

Besides the photocatalysis-induced attack, it has been reported that under UV irradiation (300-400 nm), in some kinds of bacteria (e.g. *E.coli*), O_2^- and singlet oxygen 1O_2 are generated inside the cells itself by photosensitization and lead to self-damage of bacteria, such as the DNA strand breakage or the autoxidation of lipids or other cell components (Hollaender 1943, Fujihira et al. 1982).

To make an anticipation for the future study, since UV-A/VIS light in the range of 380-495 nm has been widely used in medicine, it is of clinical interest to develop potential photocatalytic antibacterial effects in this wavelength region under therapeutically acceptable intensity and dosage (Vandersee et al. 2015). It should be noted that the radiant exitance (UVA 25 mW cm⁻²; UV-A/VIS 1050 mW cm⁻²) in this in vitro study was far above the normal therapeutical settings in the medical devices (UV 3.7 mW cm⁻²; UV-A/VIS 100 mW cm⁻²). Considering that UV light could lead to DNA-mutation, immunosuppression, photoaging and especially carcinogenesis (Kelly et al. 2000, Poon et al. 2014), and UV-A/VIS light could also cause the production of reactive oxygen species to diminish antioxidative ability of human skin (Vandersee et al. 2015). It is also worthwhile in the future to figure out if the irradiation parameters in this study need to be

modified to adapt to clinical requirement. In addition, it should be noted that, although in theory, the photon energy of the irradiation light > 385 nm is not enough to trigger photocatalysis on anatase, however, in the pilot study, the decomposition of saliva pellicle was also observed even under irradiation > 390 nm. One explanation is that, maybe the anatase coating contained certain impurities, which might have changed the photocatalytic property of the material (Shymanovska et al. 2011). Further experiments need to be done to clarify this point.

4.2. The influence of rinsing flow rate

Based on what has been shown on the microscopic fluorescent images of the reference tests I and II, it could be inferred that in this study the elevated rinsing flow rate during the irradiation period had no obvious influence on the bacterial removal. The observed bactericidal effect and bacterial removal could be attributed to the light irradiation.

Despite of this, this didn't mean that rinsing flow rate took little effect in antibacterial performance. In a study published by Sharma et al. (Sharma, Gibcus et al. 2005), it was indicated that lift forces due to fluid flow are generally too weak to cause microbial detachment. Only when the flow exceeds a critical threshold, then the resulted shear rates may be high enough to stimulate microbial detachment. However, the detachment depends on the microbial strain. In study of Sharma et al. (Sharma, Gibcus et al. 2005), fluid flow rates of 200, 235, and 300 ml min⁻¹, corresponding to wall shear rates of 11,000, 13,000 and 16,000 s⁻¹, were found being effective in detaching a hydrophilic streptococcus but not in detaching a hydrophobic actinomycetes. The cell

hydrophobicity was thought to be one factor contributing to the tenacious adhesion of actinomycetes. Similarly, the adhesive fibrils of *S. gordonii strain DL1*, which was used in our study, also conveyed the hydrophobic properties to the cell surface (McNab et al. 1999) and this might serve as one potential reason for the negligible bacterial detachment in reference I tests. What's more, in our study, the shear rate at $2700 \mu\text{L min}^{-1}$ injected fluid flow was calculated to be 2.04 s^{-1} , which was relatively too small to produce an effective microbial detachment. These might explain why the influence of the rinsing flow rate was negligible in this study.

5. Conclusions

In this study, photocatalytic antibacterial effects were investigated under different irradiation protocols on anatase. The results showed that, under UV-A ($> 320 \text{ nm}$) and UV-A/VIS threshold ($> 380 \text{ nm}$) irradiation, the photocatalytic antibacterial performance, i.e., bactericidal effects and a decreased number of adherent bacteria, could be observed by the fluorescent microscopic images. However, when the wavelength of irradiation light was limited to $> 390 \text{ nm}$, the corresponding antibacterial performance became not obvious. Considering also the results of reference tests, which were conducted on Ti surface and under UV-A irradiation, the photocatalytic antibacterial effect could be attributed to the specific property of anatase. What's more, considering the results from a pilot study, in which the photocatalytic decomposition of saliva pellicle could be observed even under 400-410 nm visible light irradiation, it is suggested that the specific photocatalytic process at the bacteria-substratum interface is more complicated and might be influenced by different factors.

Besides, it appeared that, in this study, the flow rate didn't contribute to the antibacterial performance. By calculating the hydrodynamic parameters and comparing with other reports, the shear rate values in this study were comparatively small, and this might explain its negligible influence on the bacterial adherence and detachment.

Since UV-A/VIS light in the range between 380 and 390 nm - found to attack bacteria similarly as UV-A - is much more acceptable in clinical applications than the potentially harmful, higher energetic UV-A light, it is of substantial interest to further investigate photocatalytic antibacterial effects in this wavelength region in order to develop clinically acceptable treatment protocols.

6. Summary

Anatase is a well-known photocatalytic material, in which active oxygen species can be generated under UV irradiation, and the adhered organic molecules can be decomposed through a series of oxidization reactions. The main purpose of this study was to investigate if there is sufficient photocatalytic antibacterial activity on anatase if the irradiation wavelength is shifted towards the visible light region. The quartz-crystal microbalance device (QCM-D; D-300, Q-Sense, Sweden) was used in this test and it consists of 3 main parts: electronics unit for monitoring the experimental conditions, a flow cell for loading the acoustic sensors, and Q-Sense Software for recording the frequency (f) and dissipation (D) signals of the quartz oscillation. In this study, after the online deposition of salivary pellicle and *Streptococcus gordonii* (*S. gordonii*) on the anatase sensor surface, different irradiation protocols (UV-A > 320 nm; UV-A/VIS > 380 nm, > 390 nm; VIS 400-410 nm) were utilized to excite photocatalysis. Besides, the flow rate during the irradiation period was modulated between a higher (2700 μ l

min⁻¹) or basic (110 µl min⁻¹) value and two reference tests have been designed to investigate the respective influence of irradiation and shear rate on the antibacterial effect. In addition, reference tests on Ti-coated quartz crystals were conducted under UV-A irradiation and increased flow rate (2700 µl min⁻¹) to determine if antibacterial effects are restricted to photocatalytic activity or occur also directly upon UV-A. After irradiation, the quartz crystals were demounted and adhering bacteria were stained with LIVE/DEAD® BacLight™ Bacterial Viability Kit. The fluorescent staining results on the quartz crystal surfaces were microscopically analysed and documented by DLSR camera. The mean proportion of dead bacteria on the surfaces was calculated by image processing for each group. As the results, under UV-A (> 320 nm) and UV-A/VIS threshold (> 380 nm) irradiation, a photocatalytic antibacterial performance, i.e., bactericidal effects and decreased numbers of adherent bacteria, could be observed. However, when the wavelength of irradiation light was limited to > 390 nm, a significant antibacterial performance could not be observed. The photocatalytic antibacterial effect could be attributed to the specific property of anatase. Since UV-A/VIS light in the range between 380 and 390 nm - found to attack bacteria similarly as UV-A - is much more acceptable in clinical applications than the potentially harmful, higher energetic UV-A light, it is of substantial interest to further investigate photocatalytic antibacterial effects in this wavelength region in order to develop clinically acceptable treatment protocols.

7. Zusammenfassung

Anatas ist ein bekanntes fotokatalytisches Material, in dem aktive Sauerstoffspezies unter UV-Einstrahlung generiert werden können und die

angehafteten organischen Moleküle können über eine Reihe von Oxidierungsprozessen zerlegt werden. Die Hauptaufgabe dieser Studie war es, zu untersuchen, ob ausreichend fotokatalytische antibakterielle Aktivitäten auf Anatas vorhanden sind, wenn die Wellenlänge der Einstrahlung zur sichtbaren Lichtregion verschoben wird. Das Mikrowaagengerät mit Quarzkristallen (QCM-D; D-300, Q-Sense, Schweden) wurde in diesem Test verwendet und es besteht aus 3 Hauptteilen: einer Elektronikeinheit zur Überwachung der experimentellen Bedingungen, einer Durchflusszelle für das Laden der akustischen Sensoren und der Q-Sense Software zur Aufzeichnung der Frequenz (f) und der Dissipationssignale (D) der Quarzschwingung. In dieser Studie, nach der angeschlossenen Ablage von Speichelpellikel und der *Streptococcus gordonii* (S. Gordonii) auf der Sensoroberfläche von Anatas, wurden verschiedene Einstrahlungsprotokolle (UV-A > 320 nm; UV-A/VIS > 380 nm, > 390 nm; VIS 400 – 410 nm) verwendet, um eine Fotokatalyse anzuregen. Außerdem wurde der Durchfluss während der Einstrahlungsperiode zwischen einem höheren (2700 $\mu\text{l min}^{-1}$) und einem regulären (110 $\mu\text{l min}^{-1}$) Wert angepasst. Zwei Referenztests wurden entworfen, um den jeweiligen Einfluss der Einstrahlung und der Scherrate auf den antibakteriellen Effekt zu untersuchen. Zusätzlich wurden Referenztests auf Quarzkristalle mit Ti-Beschichtung unter UV-A-Einstrahlung und einem höheren Durchfluss (2700 $\mu\text{l min}^{-1}$) durchgeführt, um zu bestimmen, ob antibakterielle Effekte nur auf die fotokatalytische Aktivität beschränkt sind, oder ob sie auch direkt während der UV-A auftreten. Nach der Bestrahlung wurden die Quarzkristalle abgebaut und die angehafteten Bakterien wurden mit dem bakteriellen Viabilitätsbausatz LIVE/DEAD® BacLight™ eingefärbt. Die fluoreszenten Färbeergergebnisse auf

den Oberflächen des Quarzkristalls wurden mikroskopisch analysiert und von einer Spiegel-Reflex-Kamera dokumentiert. Der Anteil der toten Bakterien auf den Oberflächen wurde für jede Gruppe durch Bildbearbeitung kalkuliert. Als Ergebnis dessen konnte man, unter UV-A (> 320 nm) und UV-A/VIS (> 380 nm) Einstrahlung und einer fotokatalytischen antibakteriellen Performance, bakterientötende Effekte und verminderte Zahlen von angehefteten Bakterien feststellen. Wenn allerdings die Wellenlänge der Einstrahlung auf > 390 nm beschränkt war, konnte keine signifikante antibakterielle Performance festgestellt werden. Der fotokatalytische antibakterielle Effekt konnte der besonderen Eigenschaft von Anatas zugeteilt werden. Da das UVA-A/VIS-Licht im Bereich zwischen 380 und 390 nm – es wurde herausgefunden, dass es Bakterien angreift, ähnlich wie UV-A – in klinischen Anwendungen wesentlich akzeptable ist, als das potenziell schädliche und energischere UV-A-Licht, besteht ein erhebliches Interesse, fotokatalytische antibakterielle Effekte in diesem Wellenbereich weiter zu untersuchen, um klinisch akzeptable Behandlungsprotokolle zu entwickeln.

8. References

Asahi R, Morikawa T, Ohwaki T, Aoki K and Taga Y (2001) Visible-light photocatalysis in nitrogen-doped titanium oxides. *Science* 293:269-271.

Adell R, Eriksson B, Lekholm U, Brånemark PI and Jemt T (1990) A long-term follow-up study of osseointegrated implants in the treatment of totally edentulous jaws. *Int J Oral Maxillofac Implants* 5: 347–359.

Ash A, Mulholland F, Burnett GR and Wilde PJ (2014) Structural and compositional changes in the salivary pellicle induced upon exposure to SDS and STP. *Biofouling* 30: 1183-1197.

Assender H, Bliznyuk V and Porfyrakis K (2002) How surface topography relates to materials' properties. *Science* 9: 973-976.

Barbour ME, Gandhi N, el-Turki A, O'Sullivan DJ and Jagger DC (2009) Differential adhesion of *streptococcus gordonii* to anatase and rutile titanium dioxide surfaces with and without functionalization with chlorhexidine. *J Biomed Mater Res Part A* 90A: 993-998.

Benedix R, Dehn Frank, Quaas J and Orgass Marko (2000) Application of Titanium Dioxide Photocatalysis to Create Self-Cleaning Building Materials. *LACER* 5: 157-168.

Bombeccari GP, Guzzi G, Gualini F, Gualini S, Santoro F and Spadari F (2013) Photodynamic therapy to treat periimplantitis. *Implant Dent* 6: 631-638.

Bonetta S, Bonetta S, Motta F, Strini A and Carraro E (2013) Photocatalytic bacterial inactivation by TiO₂-coated surfaces. *AMB Express* 3: 59-59.

Bowers K, Keller J, Randolph BA, Wick DG and Michaels CM (1992) Optimization of surface micromorphology for enhanced osteoblast responses in vitro. *Int J Oral Maxillofac Implants* 7: 302-310.

Brady R, Calhoun J, Leid J and Shirliff M (2009) Infections of orthopaedic implants and devices, 3: 15-55, M. Shirliff and J. Leid, *The Role of Biofilms in Device-Related Infections*. Springer- Verlag Berlin Heidelberg.

Brånemark PI, Hansson BO, Adell R, Breine U, Lindström J, Hallén O and Ohman A (1977) Osseointegrated implants in the treatment of the edentulous jaw. Experience from a 10-year period. *Scand J Plast Reconstr Surg* 16: 1-132.

Brånemark PI, Adell R and Breine U (1969) Intra-osseous anchorage of dental prostheses. *I Exp Stud Scand J Plast Reconstr Surg* 3: 81-100.

Busquim TP, May JE, Kuri SE, Nascente PAP (2010) Titanium oxide layer on the surface of anodized dental implants, 60-65, ASM International, *Medical Device Materials V: Proceedings from the Materials & Processes for Medical Devices Conference*.

Cai Y, Stromme M, Melhus A, Engqvist H and Welch K (2014) Photocatalytic inactivation of biofilms on bioactive dental adhesives. *J Biomed Mater Res B Appl Biomater* 102: 62-67.

Carré G, Hamon E, Ennahar S, Estner M, Lett MC, Horvatovich P, Gies JP, Keller V, Keller N and Andre P (2014) TiO₂ photocatalysis damages lipids and proteins in escherichia coli. *Appl Environ Microbiol* 80: 2573-2581.

Christersson CE, Glantz PO and Baier RE (1988) Role of temperature and shear forces on microbial detachment. *Scand J Dent Res* 96: 91-98.

Crawford RJ, Webb HK, Truong VK, Hasan J and Ivanova EP (2012) Surface topographical factors influencing bacterial attachment. *Advances in Colloid and Interface Science* 179–182: 142-149.

Del Curto B, Brunella MF, Giordano C, Pedferri MP, Valtulina V, Visai L and Cigada A (2005) Decreased bacterial adhesion to surface-treated titanium. *Int J Artif Organs* 28: 718-730.

Ditta IB, Steele A, Liptrot C, Tobin J, Tyler H, Yates HM, Sheel DW and Foster HA (2008) Photocatalytic antimicrobial activity of thin surface films of TiO₂, CuO and TiO₂/CuO dual layers on Escherichia coli and bacteriophage T4. *Appl Microbiol Biotechnol* 79: 127-133.

Dixon MC (2008) Quartz Crystal Microbalance with Dissipation Monitoring: Enabling Real-Time Characterization of Biological Materials and Their Interactions. *Journal of Biomolecular Techniques : JBT* 19: 151–158.

Esposito M, Hirsch J, Lekholm U and Thomsen P (1999) Differential diagnosis and treatment strategies for biologic complications and failing oral implants: a review of the literature. *Int J Oral Maxillofac Implants* 14: 473-490.

Flemming RG, Murphy CJ, Abrams GA, Goodman SL and Nealey PF (1999) Effects of synthetic micro- and nano-structured surfaces on cell behavior. *Biomaterials* 20: 573-588.

Frach P, Glöß D, Metzner C, Modes T, Scheffel B and Zywitzki O (2006) Deposition of photocatalytic TiO₂ layers by pulse magnetron sputtering and by plasma-activated evaporation. *Vacuum* 80: 679-683.

Froum SJ, Dagba AS, Shi Y, Perez-Asenjo A, Rosen PS and Wang WC (2016) Successful surgical protocols in the treatment of peri-implantitis: A narrative review of the literature. *Implant Dent* 3: 416-426.

Fujihira M, Satoh Y and Osa T (1982) Heterogeneous Photocatalytic Reactions on Semiconductor Materials. III. Effect of pH and Culons on the Photo-Fenton Type Reaction. *Bulletin of the Chemical Society of Japan* 55: 666-671.

Fujishima A and Honda K (1972) Electrochemical Photolysis of Water at a Semiconductor Electrode. *Nature* 238: 37-38.

Gopal J, George RP, Muraleedharan P and Khatak HS (2004) Photocatalytic Inhibition of Microbial Adhesion by Anodized Titanium. *Biofouling* 20: 167-175.

Gristina AG, Naylor P and Myrvik Q (1988) Infections from biomaterials and implants: a race for the surface. *Med Prog Technol* 14: 205-224.

Hayashi M, Jimbo R, Lindh L, Sotres J, Sawase T, Mustafa K, Andersson M and Wennerberg A (2012) In vitro characterization and osteoblast responses to nanostructured photocatalytic TiO₂ coated surfaces. *Acta Biomaterialia* 8: 2411-2416.

Heitz-Mayfield LJ (2008) Peri-implant diseases: diagnosis and risk indicators. *J Clin Periodontol* 35: 292-304.

Heitz-Mayfield L and Mombelli A (2014) The therapy of peri-implantitis: a systematic review. *Int J Oral Maxillofac Implants* 29: 325-345.

Heydenrijk K, Meijer JA, Van der Reijden WA, Raghoobar GM, Vissink A and Stegenga B (2002) Microbiota around root-form endosseous implants: A review of the literature. *Int J Oral Maxillofac Implants* 17:829–38.

Hollaender A (1943) Effect of long ultraviolet and short visible radiation (3500 to 4900Å) on escherichia coli. *Journal of Bacteriology* 46: 531-541.

Howe RF (1998) Recent Developments in Photocatalysis. *Developments in Chemical Engineering and Mineral Processing* 6: 55-84.

Jafari M, Jamnezhad H and Nazarzadeh L (2012) Electronic properties of titanium using density functional theory. *Iranian Journal of Science & Technology* A4: 511-515.

Jemt T, Chai J, Harnett J, Heath MR, Hutton JE, Johns RB, McKenna S, McNamara DC, van Steenberghe D, Taylor R, Watson RM and Herrmann I (1996) A 5-year prospective multicenter follow-up report on overdentures supported by osseointegrated implants. *Int J Oral Maxillofac Implants* 11: 291–298.

Jones CG (1997) Chlorhexidine: is it still the gold standard? *Periodontol* 2000 15: 55-62.

Joost U, Juganson K, Visnapuu M, Mortimer M, Kahru A, Nõmmiste E, Joost U, Kisand V and Ivask A (2015) Photocatalytic antibacterial activity of nano-TiO₂ (anatase)-based thin films: Effects on *Escherichia coli* cells and fatty acids. *J Photochem Photobiol B* 142: 178-185.

Jordan JL and Fernandez EJ (2008) QCM-D sensitivity to protein adsorption reversibility. *Biotechnology and Bioengineering* 101: 837-842.

Kaneva N, Stambolova I, Blaskov V, Dimitriev Y, Vassilev S and Dushkin C (2010) Photocatalytic activity of nanostructured ZnO films prepared by two different methods for the photoinitiated decolorization of malachite green. *J Alloys Compd* 500: 252-258.

Kelly DA, Young AR, McGregor JM, Seed PT, Potten CS and Walker SL (2000) Sensitivity to sunburn is associated with susceptibility to ultraviolet radiation-induced suppression of cutaneous cell-mediated immunity. *J Exp Med* 3: 561-566.

Kieswetter K, Schwartz Z, Hummert TW, Cochran DL, Simpson J, Dean DD and Boyan BD (1996) Surface roughness modulates the local production of growth factors and cytokines by osteoblast-like MG-63 cells. *J Biomed Mater Res* 32: 55-63.

Kikuchi Y, Sunada K, Iyoda T, Hashimoto K and Fujishima A (1997) Photocatalytic bactericidal effect of TiO₂ thin films: dynamic view of the active oxygen species responsible for the effect. *J Photochem Photobiol A Chem* 106: 51-56.

Krajewski S, Rheinlaender J, Ries P, Canjuga D, Mack C, Scheideler L, Schaffer TE, Geis-Gerstorf J, Wendel HP and Rupp F (2014) Bacterial interactions with proteins and cells relevant to the development of life-threatening endocarditis studied by use of a quartz-crystal microbalance. *Anal Bioanal Chem* 406: 3395-3406.

Langford CH (2012) Photocatalysis—A Special Issue on a Unique Hybrid Area of Catalysis. *Catalysts* 2: 327.

Lindhe J and Meyle J (2008) Peri-implant diseases: Consensus Report of the Sixth European Workshop on Periodontology. *J Clin Periodontol* 35: 282-285. Luttrell T, Halpegamage S, Sutter E and Batzill M (2014) Photocatalytic activity of anatase and rutile TiO₂ epitaxial thin film grown by pulsed laser deposition. *Thin Solid Films* 564: 146-155.

Macakova L, Yakubov GE, Plunkett MA and Stokes JR (2010) Influence of ionic strength changes on the structure of pre-adsorbed salivary films. A response of a natural multi-component layer. *Colloids Surf B Biointerfaces* 77: 31-39.

Machtei EE, Frankenthal S, Levi G, Elimelech R, Shoshani E, Rosenfeld O, Tagger-Green N and Shlomi B (2012) Treatment of peri-implantitis using multiple applications of chlorhexidine chips: a double-blind, randomized multi-centre clinical trial. *J Clin Periodontol* 39:1198–1205.

Maness PC, Smolinski S, Blake DM, Huang Z, Wolfrum EJ and Jacoby WA (1999) Bactericidal activity of photocatalytic TiO₂ reaction: toward an understanding of its killing mechanism. *Appl Environ Microbiol* 65: 4094-4098.

Martin J, Schwartz Z, Hummert TW, Schraub DM, Simpson J Jr, Dean DD, Cochran DL, Boyan BD (1995) Effect of titanium surface roughness on proliferation, differentiation, and protein synthesis of human osteoblast-like cells (MG63). *J Biomed Mater Res* 29: 389-401.

Matsunaga T, Tomoda R, Nakajima T and Wake H (1985) Photoelectrochemical sterilization of microbial cells by semiconductor powders. *FEMS Microbiology Letters* 29: 211-214.

McNab R, Forbes H, Handley PS, Loach DM, Tannock GW and Jenkinson HF (1999) Cell Wall-Anchored CshA Polypeptide (259 Kilodaltons) in *Streptococcus gordonii* Forms Surface Fibrils That Confer Hydrophobic and Adhesive Properties. *Journal of Bacteriology* 181(10): 3087-3095.

Mitoraj D, Janczyk A, Strus M, Kisch H, Stochel G, Heczko PB and Macyk W (2007) Visible light inactivation of bacteria and fungi by modified titanium dioxide. *Photochem. Photobiol. Sci* 6: 642-648.

Mombelli A, Muller N and Cionca N (2012) The epidemiology of peri-implantitis. *Clin Oral Implants Res* 23 Suppl 6: 67-76. Muszkat L, Feigelson L, Bir L and Muszkat KA (2002) Photocatalytic degradation of pesticides and bio-molecules in water. *Pest Manag Sci* 58: 1143-1148.

Niinomi M (1998) Mechanical properties of biomedical titanium alloy. *Mat Sci Eng A* 243: 231–236.

Niinomi M (2003) Recent research and development in titanium alloys for biomedical applications and healthcare goods. *Sci Technol Adv Mater* 4: 445-454.

Olsson AL, van der Mei HC, Busscher HJ and Sharma PK (2011) Acoustic sensing of the bacterium-substratum interface using QCM-D and the influence of extracellular polymeric substances. *J Colloid Interface Sci* 357: 135-138.

Oplaender C, Deck A, Volkmar M, Kirsch M, Liebmann J, Born M, van Abeelen F, van Faassen EE, Kroencke KD, Windolf J and Suschek CV (2013) Mechanism and biological relevance of blue-light (420-453 nm)

induced nonenzymatic nitric oxide generation from photolabile nitric oxide derivatives in human skin in vitro and in vivo. *Free Radic Biol Med* 65: 1363-1377.

O'Regan B and Gratzel M (1991) A low-cost, high-efficiency solar cell based on dye-sensitized colloidal TiO₂ films. *Nature* 353: 737-740.

Osman RB, Swain MV (2015) A critical review of dental implant materials with an emphasis on titanium versus zirconia. *Materials* 8: 932-958.

Parmar D, Hauman CHJ, Leichter JW, McNaughton A and Tompkins GR (2011) Bacterial localization and viability assessment in human ex vivo dentinal tubules by fluorescence confocal laser scanning microscopy. *Int Endod J* 44: 644-651.

Parr GR, Gardner LK and Toth RW (1985) Titanium: The mystery metal of implant dentistry. Dental materials aspect. *J Prosthet Dent* 54: 410-414.

Plummer C and Douglas CWI (2006) Relationship between the ability of oral streptococci to interact with platelet glycoprotein Iba and with the salivary low-molecular-weight mucin, MG2. *FEMS Immunology & Medical Microbiology* 48: 390-399.

Poon F, Kang S and Chien AL (2015) Mechanisms and treatments of photoaging 2: 65-74.

Prathapachandran J and Suresh N (2012) Management of peri-implantitis. *Dental Research Journal* 9: 516-521.

Puleo D A and Nanci A (1999) Understanding and controlling the bone-implant interface. *Biomaterials* 20: 2311-2321.

Ramya S, George RP, Subba Rao RV and Dayal RK (2010) Effect of biofouling on anodized and sol-gel treated titanium surfaces: a comparative study. *Biofouling* 26: 883-891.

Rupp F, Scheideler L, Rehbein D, Axmann D and Geis-Gerstorfer J (2004) Roughness induced dynamic changes of wettability of acid etched titanium implant modifications. *Biomaterials* 25: 1429-1438

Quirynen M, De Soete M and van Steenberghe D (2002) Infectious risks for oral implants: a review of the literature. *Clin Oral Implants Res* 13: 1-19.

Renvert S, Polyzois I and Maguire R (2009) Re-osseointegration on previously contaminated surfaces: a systematic review. *Clin Oral Implants Res* 20: 216-227.

Rupp F, Haupt M, Klostermann H, Kim HS, Eichler M, Peetsch A, Scheideler L, Doering C, Oehr C, Wendel HP, Sinn S, Decker E, von Ohle C and Geis-Gerstorfer J (2010) Multifunctional nature of UV-irradiated nanocrystalline anatase thin films for biomedical applications. *Acta Biomaterialia* 6: 4566-4577.

Rupp F, Scheideler L, Rehbein D, Axmann D and Geis-Gerstorfer J (2004) Roughness induced dynamic changes of wettability of acid etched titanium implant modifications. *Biomaterials* 25: 1429-1438.

Rupp F, Haupt M, Eichler M, Doering C, Klostermann H, Scheideler L, Lachmann S, Oehr C, Wendel HP, Decker E, Geis-Gerstorfer J and von Ohle C (2012) Formation and photocatalytic decomposition of a pellicle on anatase surfaces. *J Dent Res* 91: 104-109.

Sahrman P, Ronay V, Hofer D, Attin T, Jung RE and Schmidlin PR (2015) In vitro cleaning potential of three different implant debridement methods. *Clin Oral Implants Res* 26: 314-319.

Sauerbrey G (1959) Verwendung von Schwingquarzen zur Wägung dünner Schichten und zur Mikrowägung. *Zeitschrift für Physik* 155: 206-222.

Schaer D, Ramseier CA, Eick S, Arweiler NB, Sculean A and Salvi GE (2013) Anti-infective therapy of peri-implantitis with adjunctive local drug delivery or photodynamic therapy: six-month outcomes of a prospective randomized clinical trial. *Clin Oral Implants Res* 1: 104-110.

Schwarz F, Schmucker A and Becker J (2015) Efficacy of alternative or adjunctive measures to conventional treatment of peri-implant mucositis and peri-implantitis: a systematic review and meta-analysis. *Int J Implant Dent* 1: 22.

Sclafani A and Herrmann JM (1996) Comparison of the photoelectronic and photocatalytic activities of various anatase and rutile forms of titania in pure liquid organic phases and in aqueous solutions. *J Phys Chem* 100: 13655-13661.

Sharma PK, Gibcus MJ, van der Mei HC and Busscher HJ (2005) Influence of fluid shear and microbubbles on bacterial detachment from a surface. *Appl Environ Microbiol* 71(7): 3668-3673.

Shymanovska V, Kernazhitsky L, Puchkovska G, Naumov VV, Khalyavka T and Kshnyakin V (2011). The impurity ion influence on the optical and photocatalytic properties of anatase and rutile. *Journal of Nano- and Electronic Physics: JNEP* 3: 63-73.

Smith DC (1993) Dental implants: Materials and design considerations. *Int J Prosthodont* 6: 106-117. Sunada K, Watanabe T and Hashimoto K (2003) Studies on photokilling of bacteria on TiO₂ thin film. *J Photochem Photobiol A* 156: 227-233.

Tran TH, Nosaka AY and Nosaka Y (2006) Adsorption and photocatalytic decomposition of amino acids in TiO₂ photocatalytic systems. *J Phys Chem B* 110: 25525-25531.

Truong VK, Lapovok R, Estrin YS, Rundell S, Wang JY, Fluke CJ, Crawford RJ and Ivanova EP (2010) The influence of nano-scale surface roughness on bacterial adhesion to ultrafine-grained titanium. *Biomaterials* 31: 3674-3683.

Vandersee S, Beyer M, Lademann J and Darvin ME (2015) Blue-violet light irradiation dose dependently decreases carotenoids in human skin, which indicates the generation of free radicals oxidative medicine and cellular longevity 2015: 7.

Vanoyan N, Walker SL, Gillor O and Herzberg M (2010) Reduced Bacterial Deposition and Attachment by Quorum-Sensing Inhibitor 4-Nitro-pyridine-N-oxide: The Role of Physicochemical Effects. *Langmuir* 26: 12089-12094.

Visai L, De NL, Punta C, Melone L, Cigada A, Imbriani M and Arciola CR (2011) Titanium oxide antibacterial surfaces in biomedical devices. *International Journal of Artificial Organs* 34: 929-946.

Vogt BD, Lin EK, Wu WI and White CC (2004). Effect of film thickness on the validity of the Sauerbrey equation for hydrated polyelectrolyte films. *J Phys Chem B* 108: 12685-12690.

Vucko MJ, Poole AJ, Sexton BA, Glenn FL, Carl C, Whalan S and de Nys R (2013) Combining a photocatalyst with microtopography to develop effective antifouling materials. *Biofouling* 29: 751-762.

Wang D, Zhang Z, Li Y and Xu C (2014) Highly transparent and durable superhydrophobic hybrid nanoporous coatings fabricated from polysiloxane. *ACS Appl Mater Interfaces* 9:10014-10021.

Wang R, Hashimoto K, Fujishima A, Chikuni M, Kojima E, Kitamura A, Shimohigoshi M and Watanabe T (1998) Photogeneration of Highly Amphiphilic TiO₂ Surfaces. *Advanced Materials* 10: 135-138.

Wilken R, Botha SJ, Grobler A and Germishuys PJ (2001) In vitro cytotoxicity of chlorhexidine gluconate, benzydamine-HCl and povidone iodine mouthrinses on human gingival fibroblasts. *SADJ* 56: 455-460.

Wu Y, Klostermann H, Geis-Gerstorfer J, Scheideler L and Rupp F (2015) Photocatalytic effects of reactively sputtered N-doped anatase upon irradiation at UV-A and UV-A/VIS threshold wavelengths. *Surface & Coatings Technology* 272: 337-342.

Yao CS, Waterfield JD, Shen Y, Haapasalo M and MacEntee MI (2013) In vitro antibacterial effect of carbamide peroxide on oral biofilm. *J Oral Microbiol.* 5: 10.3402/jom.v3405i3400.20392.

Zitzmann NU and Berglundh T (2008) Definition and prevalence of peri-implant diseases. *J Clin Periodontol* 35: 286-291.

Zywitzki O, Modes T, Sahm H , Frach P, Goedicke K and Glöß D (2004) Structure and properties of crystalline titanium oxide layers deposited by reactive pulse magnetron sputtering. Surface and Coatings Technology 180–181: 538-543.

9. Erklärung zum Eigenanteil

Die Arbeit wurde in der Sektion Medizinische Werkstoffkunde und Technologie, Universitätsklinikum Tübingen unter verantwortlicher Betreuung von Prof. Dr. J. Geis-Gerstorfer durchgeführt.

Die wissenschaftliche Betreuung der Arbeit erfolgte durch PD Dr. Frank Rupp.

Sämtliche Experimente wurden von mir in Zusammenarbeit mit Frau Ingrid Stephan durchgeführt.

Die Verwendung der Software GIMP erfolgte nach Einarbeitung durch Herrn B. Sci. Magnus Walter.

Die statistische Auswertung erfolgte eigenständig durch mich.

Ich versichere, das Manuskript selbstständig verfasst zu haben und keine weiteren als die von mir angegebenen Quellen verwendet zu haben.

Tübingen, den

Yanyun Wu

10. Publication of the content of the dissertation

I would like to declare, the Figures 8, 9, 10, 11 and some relevant text content in this dissertation have already been published in “Wu YY, Geis-Gerstorfer J, Scheideler L and Rupp F (2016) Photocatalytic antibacterial effects on TiO₂-anatase upon UV-A and UV-A and UV-A/VIS threshold irradiation. Biofouling 32: 583-595.”, before the finish of writing this doctor dissertation.

11. Acknowledgment

I would like to express my most sincere gratitude to the following people or organizations:

Professor Dr. rer.nat. Jürgen Geis-Gerstorfer provided me the opportunity to finish my doctoral research in this department, and he supervised all of my work.

PD Dr. Frank Rupp introduced this research topic to me and guided the experimental work and publications, and he made a lot of great suggestions to improve my doctoral thesis.

PD Dr. Eva Engel reviewed my dissertation as the second reviewer.

Dr. Lutz Scheideler provided a lot of support in the biological assessment part of this work, and he also made a lot of great suggestions to improve my doctoral thesis.

Ms. Ingrid Stephan gave me great assistance in finishing all of the measurements in this study.

Ms. Cornelia Fueger and Ms. Evi Kimmerle-Mueller helped me in finishing the biological experiments.

B.Sci Magnus Walter introduced and taught me how to use the image analysis software.

My parents and brother gave me advice and encouragement all the time.

The Fraunhofer Institute for Organic Electronics, (FEP) Dresden prepared the anatase coating for this research.

The Chinese Scholarship Council provided me the financial support to pursue my study in Germany.

This work was partly supported by the International Team for Implantology Foundation (ITI, Basel, Switzerland) in the research project ITI 860-2012.